



Visible-light degradation of antibiotics catalyzed by titania/zirconia/graphitic carbon nitride ternary nanocomposites: a combined experimental and theoretical study

Peiren Ding^{a,1}, Haodong Ji^{b,1}, Peishen Li^{a,b}, Qiming Liu^c, Yunyun Wu^a, Ming Guo^a, Ziang Zhou^a, Shuai Gao^a, Wenlu Xu^a, Wen Liu^b, Qiang Wang^{a,*}, Shaowei Chen^{c,*}

^a Laboratory for Micro-sized Functional Materials & College of Elementary Education and Department of Chemistry, Capital Normal University, Beijing, 100048, PR China

^b Beijing Innovation Center for Engineering Science and Advanced Technology (BIC-ESAT) and Key Laboratory of Water and Sediment Sciences, Ministry of Education, College of Environmental Sciences and Engineering, Peking University, Beijing, 100871, PR China

^c Department of Chemistry and Biochemistry, University of California, 1156 High Street, Santa Cruz, CA, 95064, USA

ARTICLE INFO

Keywords:

TiO₂/ZrO₂/g-C₃N₄ ternary composite
heterojunction
photocatalytic degradation
visible light
berberine hydrochloride

ABSTRACT

Development of low-cost, high-performance photocatalysts for the effective degradation of antibiotics in wastewater is critical for environmental remediation. In this work, titanium dioxide/zirconium dioxide/graphitic carbon nitride (TiO₂/ZrO₂/g-C₃N₄) ternary composites are fabricated via a facile hydrothermal procedure, and photocatalytically active towards the degradation of berberine hydrochloride under visible light illumination. The performance is found to increase with the Ti:Zr atomic ratio in the nanocomposites, and obviously enhanced in comparison to that of the binary TiO₂/g-C₃N₄ counterpart, due to the formation of type I/II heterojunctions that help separate the photogenerated electron-hole pairs and produce superoxide and hydroxy radicals. The mechanistic pathways are unraveled by a deliberate integration of liquid chromatography-mass spectrometry measurements with theoretical calculations of the condensed Fukui index. Furthermore, the ecotoxicity of the reaction intermediates is examined by utilizing the Toxicity Estimation Software Tool (TEST) and quantitative structure activity relationship calculations (QSAR).

1. Introduction

With increasing global population and social development [1], environmental pollution by pharmaceuticals has been recognized as a risk to human health [2,3]. Of this, the overuse and discharge of antibiotics, such as berberine hydrochloride (BH), has been found to cause significant ecological impacts, which calls for efficient remediation strategies [4–7]. In contrast to the traditional low-efficiency treatment methods, such as precipitation, filtration, and coagulation/flocculation [8–10], a wide variety of new techniques have been reported based on, for instance, adsorption, advanced oxidation, and photocatalytic degradation [11–13]. Among these, photocatalysis has been accepted as the most effective method of treating antibiotic wastewater, due to its high efficiency in degradation and mineralization [14]. In fact, as an advanced oxidation process (AOP), photocatalysis is a promising,

environmentally benign technology, where antibiotics can be completely decomposed and mineralized into non-polluting substances, such as CO₂ and H₂O [15].

Titanium dioxide (TiO₂) is one of the most widely used photocatalysts, due to its excellent photocatalytic performance, good chemical stability, low cost, and low toxicity [16]. However, because of its relatively wide band gap of ca. 3.2 eV, TiO₂ can only be excited by ultraviolet (UV) light and exhibits low adsorption in the visible range [17]. To improve the photocatalytic performance, structural engineering of TiO₂, such as doping of select (non-)metals, represents an effective route. For instance, Samsudin et al. [18] synthesized homogeneously hydrogenated F-doped TiO₂ and exploited the synergistic interaction between hydrogen and fluorine to enhance the degradation efficiency of atrazine. Wu et al. [19] prepared C-doped TiO₂ and observed a narrowed band gap, apparent absorption across the UV, visible and near-infrared

* Corresponding authors.

E-mail addresses: qwchem@gmail.com (Q. Wang), shaowei@ucsc.edu (S. Chen).

¹ These authors contributed equally to this work.

range, and hence an enhanced photocatalytic activity. Wang et al. [20] found that surface defects were formed in N-doped TiO₂, which led to a lower Fermi level (E_F) than that of undoped TiO₂, reduced the energy barrier for electron transport and improved the photocatalytic performance. Payan et al. [21] reported degradation of sulfamethazine by Cu-TiO₂ functionalized single-walled carbon nanotubes. Zhao et al. [22] observed the formation of a Schottky barrier at the Ag-TiO₂ interface, which served as an electron trap, promoted the separation of photo-generated electrons and holes, and significantly enhanced the degradation of rhodamine B under visible light irradiation.

Zirconium dioxide (ZrO₂) is another common semiconductor, with significant physical and chemical stability and special electronic energy band structure. Similarly to TiO₂, the photocatalytic activity is limited under visible light excitation because of the wide band gap (>5 eV) [23]. Therefore, ZrO₂ is generally combined with other narrow-bandgap semiconductors to form a hybrid structure, such that the photocatalytic performance can be enhanced. For instance, Zhang et al. [24] synthesized TiO₂-ZrO₂ hollow sphere nanocomposites, and observed a significant photocatalytic performance under UV light. Li et al. [25] synthesized mesoporous ZrO₂-CeO₂-TiO₂, with ZrO₂ being the catalyst framework, where the thermal stability and specific surface area was markedly increased. Chen et al. [26] prepared graphitic carbon nitride (g-C₃N₄)/ZrO_{2-x} nanotube composites, and observed apparent photocatalytic degradation of tetracycline hydrochloride at an efficiency of 90.6 % under visible light.

g-C₃N₄ is a unique semiconducting polymer, exhibits a layered graphite structure, excellent electron-hole transfer, robust chemical and thermal stability, and a relatively low band gap (2.7 eV), and has been used rather extensively for visible-light photocatalysis [27,28]. Yet, due to the low specific surface area and weak van der Waals interaction between adjacent carbon nitride layers, the photocatalytic performance is compromised by strong carrier recombination [29]. Therefore, formation of nanocomposites with other semiconductors (e.g., TiO₂ and ZrO₂) has been demonstrated to lead to excellent photocatalytic performance [30,31]. For instance, Lu et al. [32] produced C-TiO₂/g-C₃N₄ nanocomposite by a hydrothermal method, and observed enhanced absorption in the visible region, due to the formation of heterojunctions. Tong et al. [33] utilized the formation of TiO₂/g-C₃N₄ interfacial junctions to facilitate interfacial electron transfer, and the synergistic interaction resulted in visible light absorption. Yu et al. [34] synthesized TiO₂/SiO₂/g-C₃N₄ ternary composites, and observed enhanced photocatalytic degradation of BH under visible light irradiation.

Herein, ternary composites based on TiO₂/ZrO₂/g-C₃N₄ (TZCN) were successfully prepared at varied molar ratios of Ti and Zr via a facile hydrothermal method, and displayed apparent photocatalytic activity towards the degradation of BH under visible light irradiation. The activity was found to increase with increasing TiO₂ loading in the composite, and the sample with a Ti:Zr ratio of 9:1 stood out as the best catalyst among the series. This was accounted for by the formation of heterojunctions that facilitated interfacial charge transfer, in consistency with spectroscopic and electrochemical measurements. Electron spin resonance (ESR) measurements suggested that superoxide radicals ($O_2^{\cdot-}$) were responsible for the BH degradation, with minor contributions from hydroxy radicals ($\cdot OH$). In addition, the degradation products were analyzed by liquid chromatography-mass spectrometry (LC-MS) measurements. In conjunction with density functional theory (DFT) calculations based on the Fukui function, the reaction sites on the BH molecules that might be attacked by free radicals were identified, from which possible degradation pathways of BH were proposed. Further analysis was carried out based on the Toxicity Estimation Software Tool (TEST) and quantitative structure activity relationship (QSAR) to examine the ecotoxicity of the degradation intermediates.

2. Experimental

2.1. Chemicals

Tetrabutyl titanate (Macklin Biochemicals), zirconium n-butoxide (Macklin Biochemicals), urea (Sinopharm), melamine (Sinopharm), methanol (Sinopharm), acetic acid (Sinopharm), and BH (Aladdin Chemicals) were of analytical grade and used as received. Water was deionized before use.

2.2. Sample preparation

The TZCN nanocomposites were synthesized via a facile hydrothermal procedure. The molar feed ratio of Ti:Zr was varied at 1:0, 9:1, 7:3, 5:5, 3:7, 1:9, and 0:1, while the total amount of Ti and Zr in the samples was fixed at 5 mmol (Table S1). Experimentally, urea (0.2 g), methanol (0.5 mL) and acetic acid (1 mL) were uniformly mixed under stirring for 15 min, into which was then slowly added tetrabutyl titanate and zirconium n-butoxide in a dropwise fashion under vigorous stirring for half an hour. The solutions were then allowed to stand for 10 h, before being dropped into a solution of 10 g melamine in 50 mL of water under stirring for half an hour. The obtained mixture was loaded into a 100 mL Teflon-lined autoclave, which was sealed and heated for 24 h at 180 °C. After the autoclave was cooled to room temperature, the pale yellow precipitates were collected, rinsed with a copious amount of water and absolute ethanol, and dried at 60 °C overnight. The dried samples were further calcined in a muffle furnace for 4 h at 500 °C, and the resulting samples were designated as TCN, TZCN-1, TZCN-2, TZCN-3, TZCN-4, TZCN-5, ZCN, respectively.

TiO₂/ZrO₂ binary composites were prepared in the same fashion at varied Ti:Zr feed ratios but without the addition of melamine. Three additional control samples were prepared in the same manner, pure TiO₂ except for the addition of zirconium n-butoxide and melamine, pure ZrO₂ except for the addition of tetrabutyl titanate and melamine, and pure g-C₃N₄ except for the addition of tetra-butyl titanate and zirconium n-butoxide.

The characterization details of the sample structures were included in the Supplementary Information.

2.3. Photocatalysis

A 300 W xenon lamp (FX300, PerfectLight) was used as the simulated sunlight in the photocatalytic degradation of BH. Experimentally, 10 mg of the nanocomposites obtained above was added to a quartz tube containing 50 mL of a BH (10 mg L⁻¹) solution. After ultrasonic treatment for 2 min, it was stirred in the dark for 30 min to reach an adsorption/desorption equilibrium. An aliquot of 1.5 mL was then extracted at a time interval of 10 min from the solution during photocatalytic degradation of BH into a centrifuge tube, and the supernatant obtained by centrifugation was subject to UV-vis absorption measurements. The degradation rate of BH was quantified by C/C_0 , where C_0 represents the initial BH concentration after the adsorption-desorption equilibrium, and C the BH concentration at a certain reaction time point. To examine the contributions of free radicals to the degradation of BH, 0.5 mL of *p*-benzoquinone (*p*-BQ, 0.5 mM), ammonium oxalate (AO, 1 mM), or *tert*-butanol (TBA) was loaded into the solution to quench superoxide radicals ($O_2^{\cdot-}$), photo-produced holes (h^+), or hydroxyl radicals ($\cdot OH$), respectively [35].

2.4. Recycling tests

The durability of the photocatalysts was examined by repeating the photocatalytic experiment 5 times. After each test, the photocatalyst was harvested, rinsed extensively with ethanol, dried at 60 °C, and used for the next cycle.

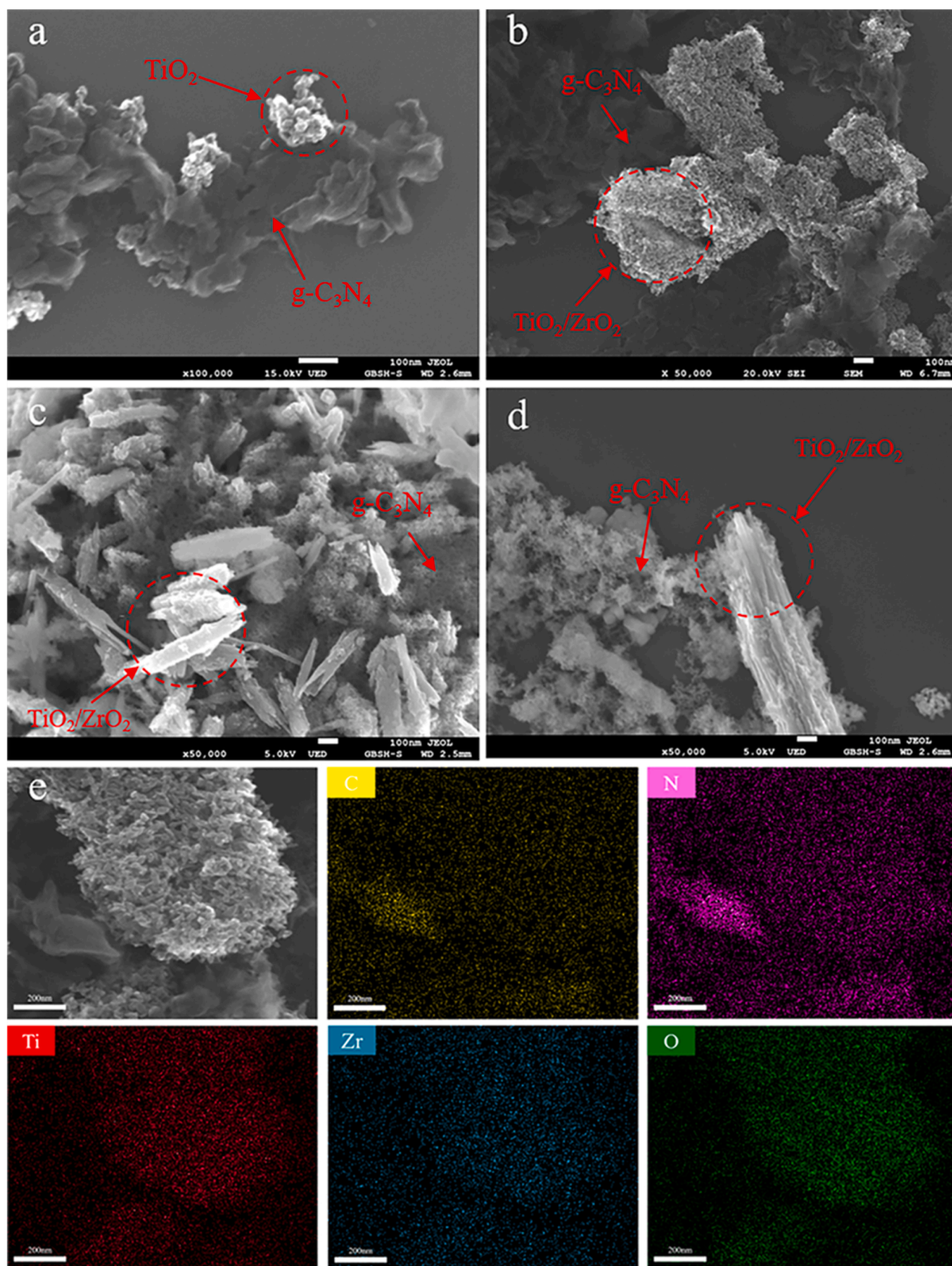


Fig. 1. SEM micrographs of (a) TCN, (b) TZCN-1, (c) TZCN-2, and (d) TZCN-3. (e) Elemental maps of C, N, Ti, Zr and O of the selected area of TZCN-1 based on EDS measurements.

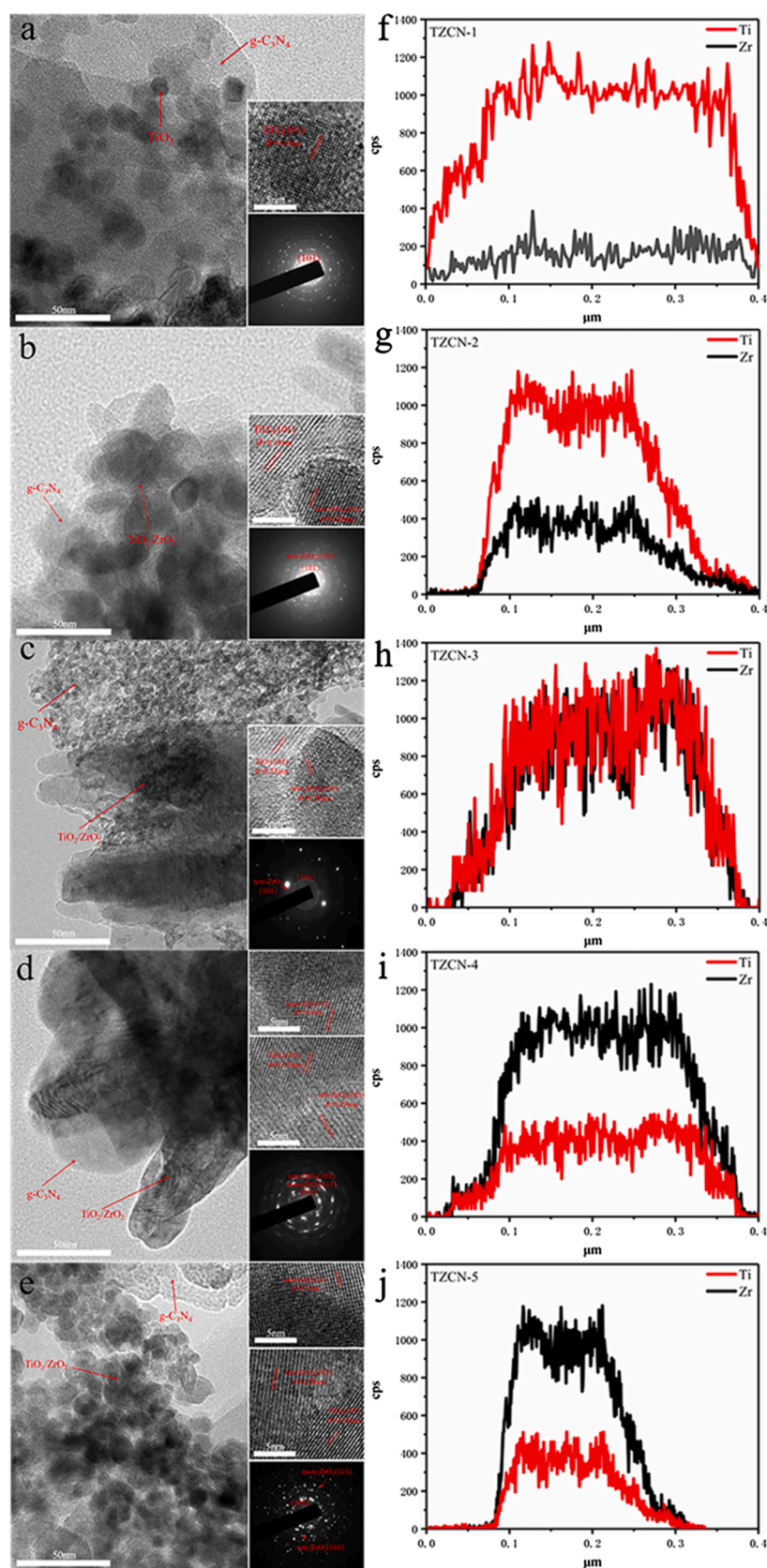


Fig. 2. (a-e) TEM images of TZCN nanocomposites and (h-j) EDS line scans: (a,f) TZCN-1, (b,g) TZCN-2, (c,h) TZCN-3, (d,i) TZCN-4, (e,j) TZCN-5. The upper insets to panels (a-e) are the high-resolution TEM images, and bottom insets are the respective SAED patterns.

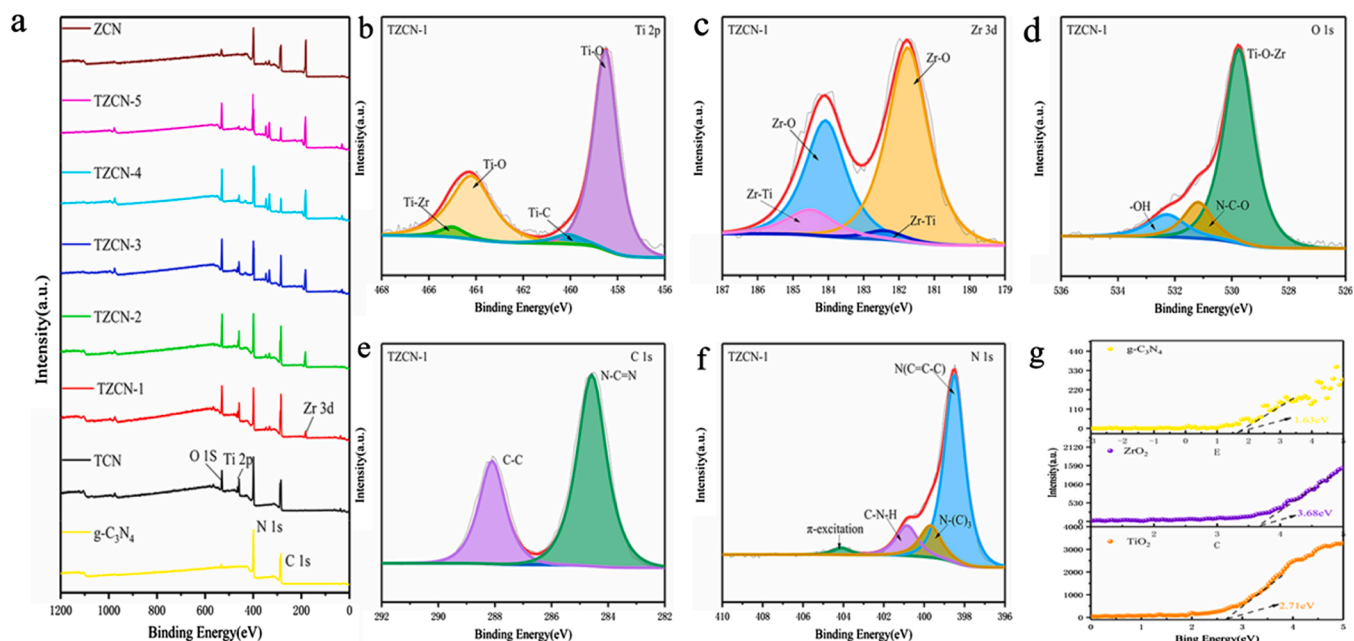


Fig. 3. (a) XPS survey spectra of the composite samples. High-sensitivity scans of the (b) Ti 2p, (c) Zr 3d, (d) O 1s, (e) C 1s, (f) N 1s, and (f) N 1s electrons of TZCN-1. (g) VB-XPS spectra of TiO_2 , ZrO_2 , and $\text{g-C}_3\text{N}_4$.

2.5. Photoelectrochemistry

A traditional three-electrode system was used for the photoelectrochemical experiments, with a saturated calomel electrode (SCE) as the reference electrode, a platinum wire as the counter electrode, and 0.1 M Na_2SO_4 as the supporting electrolyte. To prepare the working electrode, 5 mg of the nanocomposites obtained above was dispersed in 1 mL of ethanol under sonication for 10 min to form a homogeneous suspension, 0.1 mL of which was then dropcast onto a piece of FTO glass ($1\text{ cm} \times 3\text{ cm}$) and dried overnight at 60°C before use. The 300 W xenon lamp was utilized to provide the visible light source.

2.6. DFT calculations

Theoretical calculations were conducted based on the Gauss 09 package [36,37]. Details of the calculations of the condensed Fukui index [38] and TEST and QSAR analyses were included in the Supplementary Information.

3. Results and discussion

3.1. Sample structures

The structures of the prepared photocatalysts were first characterized by X-ray diffraction (XRD) measurements (Fig. S1a). One can see that $\text{g-C}_3\text{N}_4$ displayed two clearly-defined peaks at $2\theta = 13.2^\circ$ and 27.4° , due to the $\text{g-C}_3\text{N}_4$ (100) and (002) diffractions, respectively, of the periodic triazine units and aromatic system (JCPDS No. 87-1526) [39–41]. For the nanocomposites, a series of diffraction patterns can be identified for anatase TiO_2 , at $2\theta = 25.4^\circ$ (101), 38.1° (004), 48.2° (200), 54.0° (105), 55.2° (211) and 62.7° (204) (JCPDS No. 21-1272); and ZrO_2 of the monoclinic (JCPDS No. 86-1451) and tetragonal (JCPDS No. 50-1089) phases can be observed at $2\theta = 24.27^\circ$, 28.52° , 30.36° , 31.55° , 35.53° , 50.28° , and 59.96° [42,43]. With the decrease of the initial Ti:Zr feed ratio (i.e., from TCN to TZCN and ZCN), the intensity of the anatase TiO_2 diffraction peaks diminishes accordingly, whereas the diffraction peaks of zirconia (in both monoclinic and tetragonal phases) become intensified (except for TZCN-3 where no obvious zirconia diffraction peak can be observed, likely due to the formation of poorly crystalline

zirconia) [44–46]. In addition, in these nanocomposites, the $\text{g-C}_3\text{N}_4$ diffraction peaks became markedly reduced, likely because of the amorphous state of $\text{g-C}_3\text{N}_4$ in the samples [47].

Further structural insights were obtained in FTIR measurements. From Fig. S1b, the prepared composites can be seen to exhibit a series of vibrational features. The N-H vibration can be found at $3000 - 3500\text{ cm}^{-1}$ (region i) [48]. The peaks in region ii ($1200 - 1650\text{ cm}^{-1}$) are most likely due to the C-N/C=N tensile vibrations of the heterocyclic ring [49]. The s-triazine ring vibrations can be found around 808 cm^{-1} (region iii) [50]; and the peak at 780 cm^{-1} (region iv) is likely due to Zr-O vibration [51]. As the content of zirconium increases, the Zr-O stretching vibration becomes intensified. For the TZCN ternary composites, there is also a group of broad bands within the range of 400 to 700 cm^{-1} , arising from the Ti-O-Ti vibrations [52,53]. These results are in good agreement with the successful incorporation of TiO_2 , ZrO_2 and $\text{g-C}_3\text{N}_4$ into the TZCN composites.

The porosity of the nanocomposites was then quantified by analysis of the N_2 adsorption-desorption isotherms. From Fig. S1c and S1d, all samples manifested an H_3 hysteresis loop and a type-IV isotherm, suggesting the formation of a mesoporous structure. The specific surface area, pore size and volume were then estimated and summarized in Table S2. Among the series, TZCN-1 exhibited the largest specific surface area ($188.65\text{ m}^2\text{ g}^{-1}$), pore size (15.71 nm) and pore volume ($0.4824\text{ cm}^3\text{ g}^{-1}$), likely due to the cross-linked structure of nano- TiO_2 on the surface of $\text{g-C}_3\text{N}_4$ [54]. In addition, one can see from Fig. S2 that the specific surface area of the $\text{g-C}_3\text{N}_4$ -free $\text{TiO}_2/\text{ZrO}_2(9:1)$ sample was much larger than those of pure TiO_2 and ZrO_2 (Table S2), with a much narrower pore size distribution in the range of 10 to 20 nm , suggesting minimal contributions of $\text{g-C}_3\text{N}_4$ nanosheets to the nanocomposite porosity. Note that a high specific surface area and pore volume is expected to promote ready access to the photocatalytic reactive sites (vide infra).

Scanning electron microscopy (SEM) and transmission electron microscopy (TEM) measurements were then performed to examine the morphology of the prepared nanocomposites. From Fig. 1 and S3, the surface morphology of the samples can be seen to vary significantly. In contrast to the rather smooth surface of TCN (Fig. 1a) and $\text{g-C}_3\text{N}_4$ (Fig. S3d), the TZCN-1 composite exhibited a layered, and markedly roughened surface (Fig. 1b-1d), consistent with the formation of a

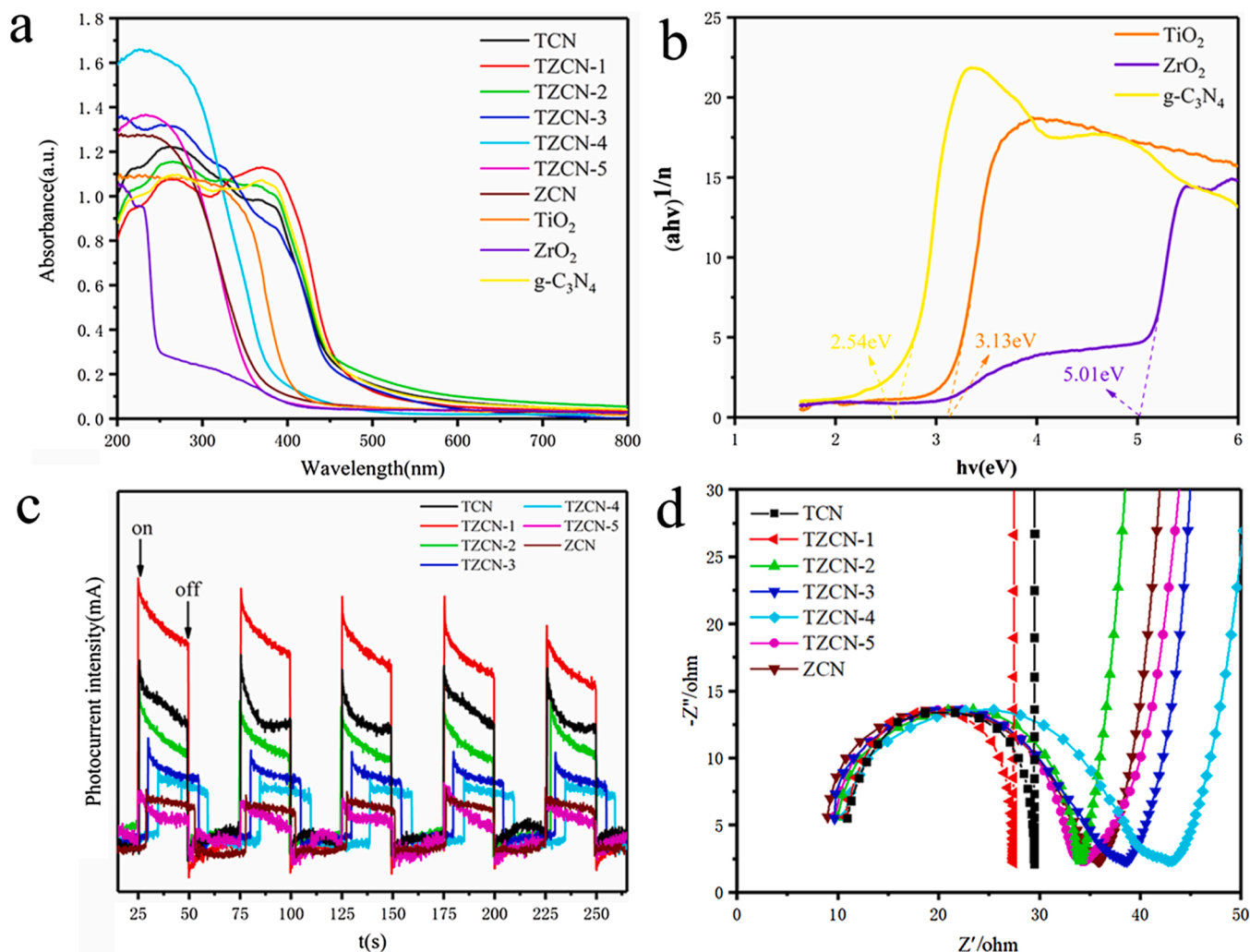


Fig. 4. (a) UV-vis DRS spectra of the sample series. (b) Tauc plots of TiO₂, ZrO₂, and g-C₃N₄. (c) Transient photocurrent profiles and (d) Nyquist plots of the sample series.

mesoporous structure (Table S2). For TZCN-2 (Fig. 1c) and TZCN-3 (Fig. 1d), the composites can be found to consist of nanoparticles and rod-like structures. Nanorods can also be found with TZCN-4 (Fig. S3a), whereas mostly particles for TZCN-5 (Fig. S3b); and for ZCN that contains only ZrO₂ (Fig. S3c), only spherical particles were produced. Such a morphological discrepancy among the sample series likely arose from a stronger affinity of TiO₂ to the g-C₃N₄ nanosheets than ZrO₂. Notably, for the g-C₃N₄-free samples of TiO₂, ZrO₂, and TiO₂/ZrO₂ composites (Fig. S4), no flaky structure was formed and the samples were found to entail extensive agglomeration of particulate structures. Furthermore, elemental mapping analysis based on EDS measurements shows an even distribution of the C, N, O, Ti, and Zr elements within TZCN-1 (Fig. 1e), confirming successful production of ternary oxide composites.

Further structural insights were obtained by TEM measurements. For TCN (Fig. S5a) and ZCN (Fig. S5b), the composites can be seen to consist of spherical TiO₂/ZrO₂ nanoparticulates supported on g-C₃N₄ nanosheets (Fig. S5c), forming a layered structure, which is further corroborated in high-resolution TEM measurements and selected area electron diffraction (SAED) studies (insets to Fig. S5a and S5b). By contrast, the TZCN nanocomposites (Fig. 2a-e) all featured a flaky structure consisting of TiO₂/ZrO₂ layers supported on g-C₃N₄ nanosheets, except for TiO₂/ZrO₂ in TZCN-5 (Fig. 2e) which showed a nanoparticulate structure, consistent with results from SEM measurements (Fig. 1 and S3). Notably, from the high-resolution TEM images in the upper insets to Fig. 2a-e, heterojunctions between g-C₃N₄, TiO₂, and ZrO₂ can be readily

identified, and the lattice fringes with an interplanar distance of 0.350, 0.290 and 0.31 nm can be ascribed to anatase TiO₂(101), tetragonal ZrO₂(101), and monoclinic ZrO₂(111) crystal facets, respectively [55]. Due to the amorphous nature of g-C₃N₄, no obvious lattice fringes were observed [31]. Consistent results were obtained in SAED measurements, as manifested in the lower insets to Fig. 2a-e, all of which display polycrystalline patterns, in excellent agreement with the XRD patterns presented in Fig. S1a. Furthermore, EDS measurements (Fig. 2f-j) showed that the Ti:Zr molar ratio was in excellent agreement with the initial feed ratio in sample preparation (Table S1).

The chemical composition of the prepared nanocomposites was then characterized by X-ray photoelectron spectroscopy (XPS) analysis. The survey spectra of the series of nanocomposites are depicted in Fig. 3a, in which the elements of C, N, O, Ti, and Zr can be readily identified at ca. 285.3, 399.2, 530.2, 459.0, and 180.8 eV, respectively. The integrated peak areas were then used to quantify the elemental compositions of the samples, where the Ti:Zr ratio can be found to be consistent with the initial molar feed ratio (Table S1 and S3). Fig. 3b illustrates the high-resolution scan of the Ti 2p electrons in TZCN-1. Two peaks can be deconvoluted at 464.4 and 458.7 eV, corresponding to the Ti 2p_{3/2} and 2p_{1/2} electrons of TiO₂ [56]. Two additional peaks can be resolved, at 465.0 eV for Ti-Zr and 460.1 eV for Ti-C [57]. Similar results were obtained in the corresponding Zr 4d scan (Fig. 3c), which can be deconvoluted into two doublets. The major doublet (182.2/184.4 eV) is due to the 3d_{3/2} and 3d_{5/2} electrons of Zr(IV) in ZrO₂ [58]; and the minor one at

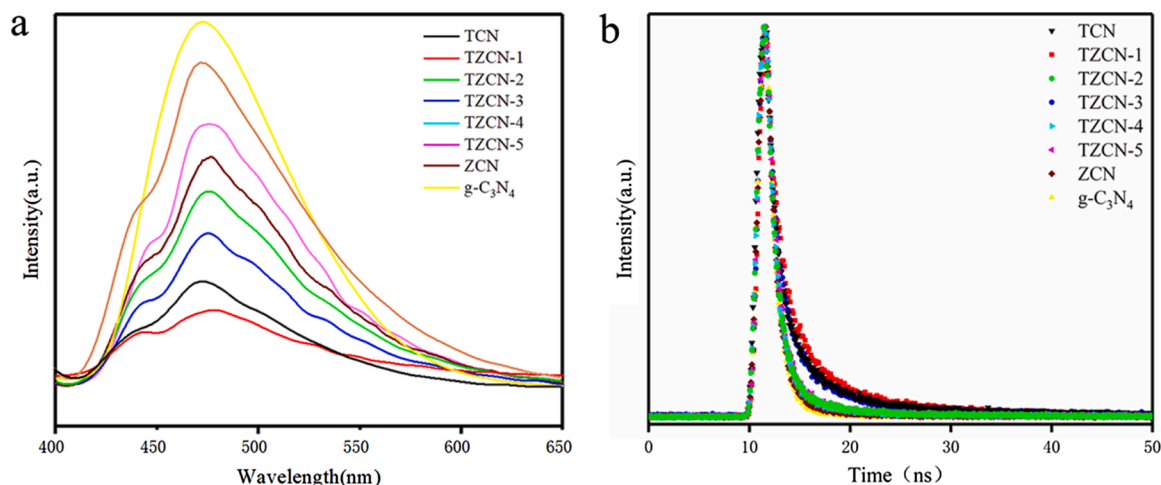


Fig. 5. (a) Steady-state and (b) time-resolved emission spectra of the sample series at the excitation of 410 nm.

182.3/184.4 eV to Zr-Ti [51,59]. Fig. 3d shows the O 1s high-resolution scan, where lattice oxygen of TiO₂/ZrO₂ can be resolved at 529.8 eV, N-C-O at 531.2 eV, and -OH at 532.2 eV [31,60,61]. The formation of Zr-O, Ti-O and Zr-Ti linkages suggests intimate interactions between TiO₂, ZrO₂ and g-C₃N₄ [62]. Fig. 3e displays the high-resolution scan of the C 1s electrons, from which C-C and N-C=N can be deconvoluted at 284.58 and 288.10 eV, respectively [63]. From the high-resolution scan of the N 1s electrons (Fig. 3f), four peaks were resolved at 398.50 eV for N(C=N-C), 399.55 eV for tertiary nitrogen N-(C)₃, 400.75 eV for C-N-H, and 404.18 eV for π excitation [64–66].

Notably, TZCN-1 exhibited a low contact angle of only 20.287° (Fig. S6), most likely because of the hydroxyl moieties on the nanocomposite surface (Fig. 3d). This unique property is conducive to interactions with BH dissolved in water and may promote the photocatalytic degradation of BH (vide infra).

Furthermore, from the XPS measurements (Fig. 3g), the valence band maximum (VBM) was estimated to be 2.71 eV for TiO₂, 3.68 eV for ZrO₂, and 1.63 eV for g-C₃N₄ [67], corresponding to 2.15, 3.12, and 1.07 V vs. normal hydrogen electrode (NHE), respectively [68–70].

UV-vis diffuse reflection spectroscopy (DRS) analysis was then performed to examine the band structure and interfacial charge transfer. From Fig. 4a, one can see that the TCN, TZCN-1, TZCN-2, TZCN-3, and g-C₃N₄ samples all show an obvious visible light absorption edge beyond 500 nm, while TZCN-4, TZCN-5 and ZCN that contain a high Zr content are mostly limited to the UV region (< 400 nm), likely due to the large

bandgap of ZrO₂ [71]. The Tauc plots of TiO₂, ZrO₂ and g-C₃N₄ are depicted in Fig. 4b, $(\alpha h\nu)^{1/n} = A(h\nu - E_g)$, where α represents the light absorption constant, ν the photon frequency, h the Planck constant, E_g the band gap energy, and n a constant determined by the type of the semiconductors [72] ($n = 2$ for TiO₂ and g-C₃N₄ [73,74] and 0.5 for ZrO₂ [75]). From the data, the bandgaps of TiO₂, ZrO₂ and g-C₃N₄ were calculated to be 3.13, 5.01, and 2.54 eV, respectively. In combination with the VBM determined from XPS measurements (Fig. 3g), the conduction band minimum (CBM) of TiO₂, ZrO₂, and g-C₃N₄ of TZCN was estimated to be -0.98, -1.47 and -1.89 V, respectively. These results suggest that the formation of ternary composites not only enhanced light absorption in the visible range, but also retained the high reduction activity of TZCN.

Consistent results were obtained in photoelectrochemical measurements of the transient photocurrents, which is a unique testing method for estimating the migration efficiency of photoproducted charge carriers [76]. From Fig. 4c and S7a, it can be seen that the sample series all show a stable and rapid photocurrent response under five repeated irradiations with a Xenon lamp. Among them, TZCN-1 shows the greatest photocurrent, which corresponds to the best photocatalytic performance, as detailed below.

A similar conclusion can be reached in electrochemical impedance spectroscopic (EIS) measurements [77]. From the Nyquist plots in Fig. 4d and S7b, TZCN-1 can be seen to exhibit the smallest semicircle diameter, suggesting a lowest charge-transfer resistance among the

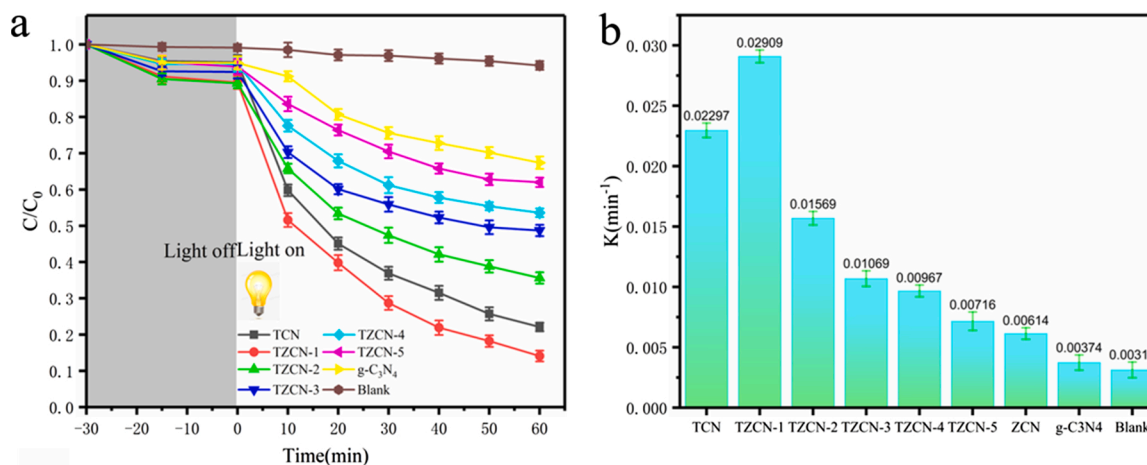


Fig. 6. (a) Photocatalytic degradation of BH by the sample series and (b) the corresponding reaction rate constants. BH concentration 20 mg L⁻¹, pH = 6.88, and catalyst loading 0.2 g·L⁻¹.

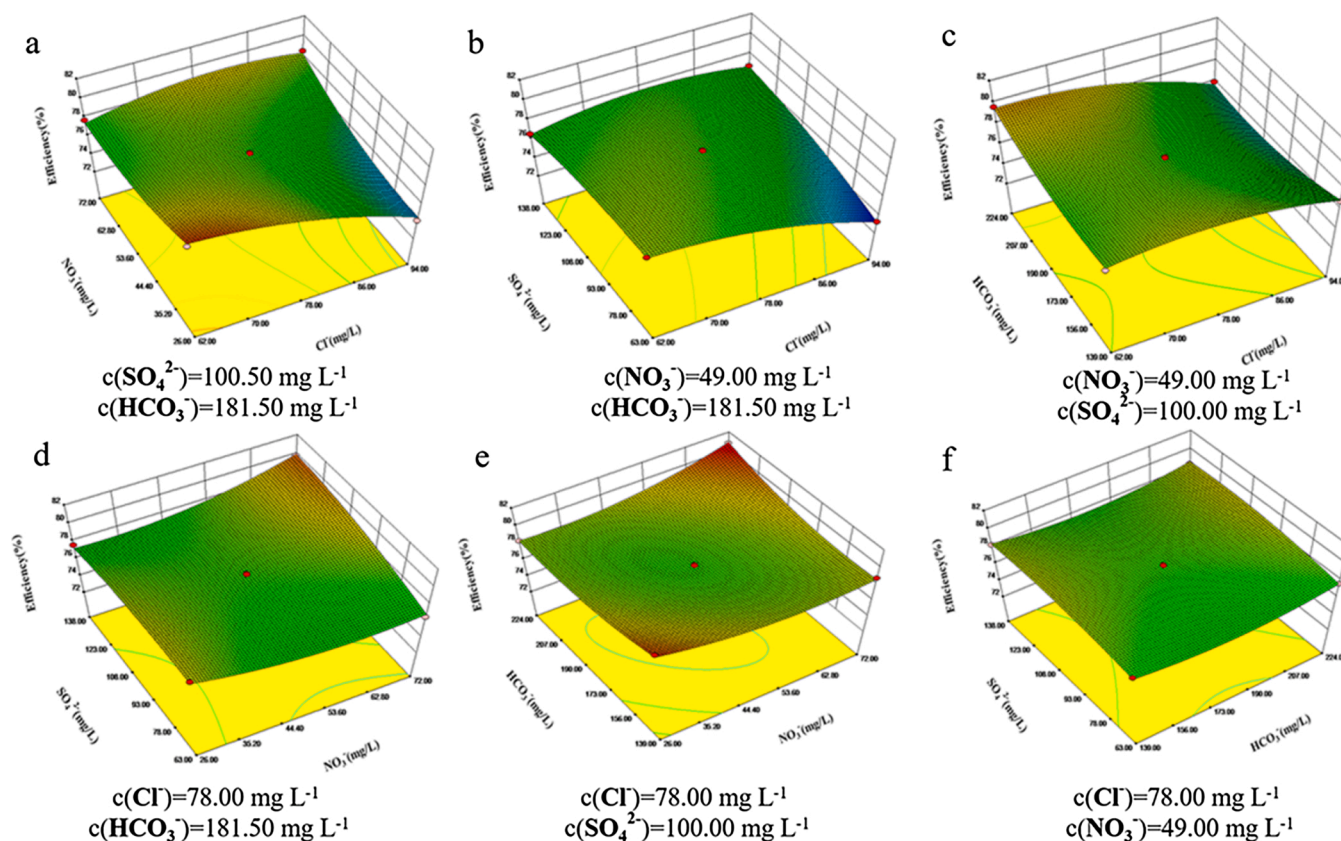


Fig. 7. Surface response plots of the photocatalytic efficiency of BH removal with the addition of different anions (Cl⁻, NO₃⁻, SO₄²⁻, HCO₃⁻) in simulated urban water.

samples, in agreement with the transient photocurrent results in Fig. 4c.

Photoluminescence (PL) studies in both steady-state and time-resolved modes further verify the effective separation of electron-hole pairs in TZCN-1 [78,79]. From Fig. 5a one can see that at the excitation of 410 nm, while the sample series all exhibit a similar emission peak at 460 nm, TZCN-1 exhibited a significantly lower emission intensity than others, indicating inhibited recombination and high-efficiency separation of photogenerated electrons and holes [80]. Indeed, in time-resolved PL measurements, upon the excitation of 410 nm, TZCN-1 shows the slowest decay of the emission (Fig. 5b). Table S4 lists the calculated decay time constant by multi-exponential fitting, where one can see that TZCN-1 features the longest (average) decay time constant (τ_A) of 15.82 ns among the sample series. Note that a long PL emission lifetime is advantageous for electron-hole separation, most likely at the heterojunction interface of the nanocomposites [78,81], a key step in photocatalytic reactions.

3.2. Photocatalytic degradation of BH

Remarkably, the prepared nanocomposites exhibited excellent photocatalytic activity towards BH degradation [82], which was conducted at the optimal pH of 6.88 (Fig. S8a) and nanocomposite concentration of 0.2 g·L⁻¹ (Fig. S8b). From Fig. 6a, one can see that (i) there is virtually no self-degradation of BH without the catalyst; (ii) upon the addition of the prepared nanocomposites, effective degradation of BH occurs; and (iii) at increasing Ti content, the photocatalytic performance of the TZCN nanocomposites increases accordingly. Specifically, after 60 min's visible photoirradiation, the degradation rate of BH is 79.93% for TCN, 86.93% for TZCN-1, 85.96% for TZCN-2, and 64.47% for TZCN-3, 51.32% for TZCN-4, 46.47% for TZCN-5, 32.68% for TCN, and only 21.75% for g-C₃N₄. That is, the TZCN-1 sample stood out with the best photocatalytic performance among the series. As the degradation reaction of BH conformed to the pseudo-first order kinetics, the reaction rate

constant (k) was found to be the highest with TZCN-1 at 0.02909 min⁻¹ among the series (Fig. 6b).

The Box-Behnken experimental method was then employed to probe the impacts of inorganic ions in urban water on the photocatalytic degradation and removal of BH. For cations like Na⁺, K⁺, Ca²⁺ and NH₄⁺ that are widely found in actual urban water, no significant impact on the photocatalytic removal of BH was observed (Fig. S8c), likely because these cations are chemically inert to photogenerated electrons and holes [72,83]. For anions like Cl⁻, NO₃⁻, SO₄²⁻ and HCO₃⁻ that are also common in urban water, substantial effects on the photocatalytic removal efficiency of BH were observed, where the anion concentration ranges and level settings were based on literature results and the inorganic ion concentrations in various areas within the City of Beijing. The ion concentration ranges and levels (4 factors), experimental independent variables and dependent variable (29 runs) are listed in Table S5 and S6. The response result (efficiency %) and the dependent variables (ion concentrations, mg L⁻¹) can be described with a polynomial equation, $\text{efficiency}(\%) = 77.79 - 1.20A + 0.24B + 0.43C + 0.083D + 1.63AB + 1.32AC - 0.66AD + 1.12BC + 1.05BD + 0.092CD - 1.06A^2 + 0.93B^2 - 0.51C^2 + 0.82D^2$. Based on the results of ANOVA analysis (Table S7), the R² and adjusted R² were estimated to be 0.9852 and 0.9703, respectively, suggesting that the response results obtained by the simulation experiment were consistent with the Box-Behnken expected values. Meanwhile, the F-values of the dependent variable of Cl⁻, NO₃⁻, SO₄²⁻ and HCO₃⁻ were 220.87, 8.75, 28.92, and 1.04, respectively, demonstrating that the four variables affected the photocatalytic removal of BH in the order of Cl⁻ > SO₄²⁻ > NO₃⁻ > HCO₃⁻. That is, Cl⁻ showed the highest influence on the photocatalytic performance. The three-dimensional surface response plots of the four anions are shown in Fig. 7. The optimal removal efficiency of BH was estimated by the Box-Behnken method, with the concentration of Cl⁻ at 78.00 mg L⁻¹, NO₃⁻ at 72.00 mg L⁻¹, SO₄²⁻ at 100.50 mg L⁻¹, and HCO₃⁻ at 224.00 mg L⁻¹.

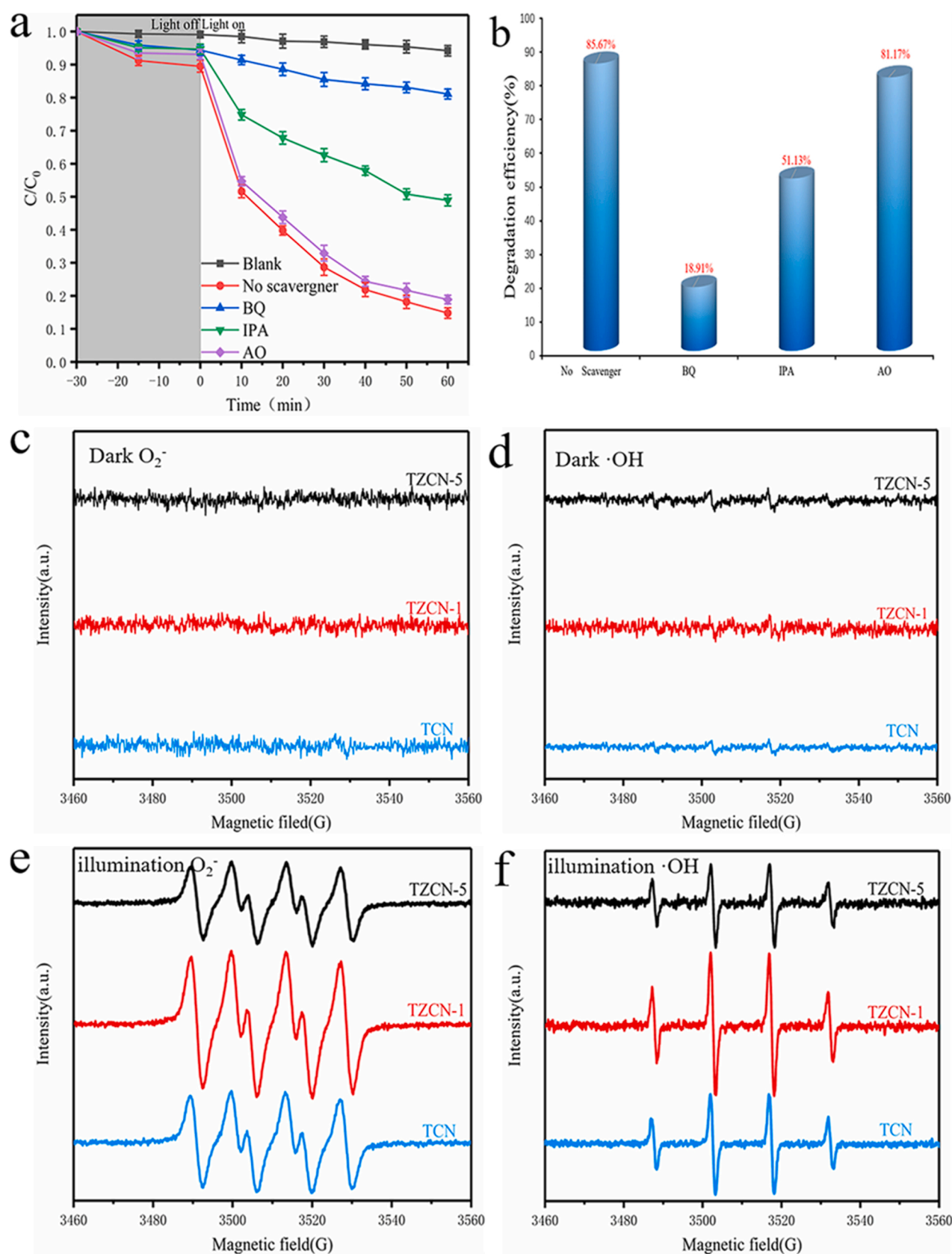


Fig. 8. (a) and (b) Influence of radical quenchers on BH degradation by TZCN-1. ESR spectra of various nanocomposites (c,d) without and (e,f) with visible light illumination.

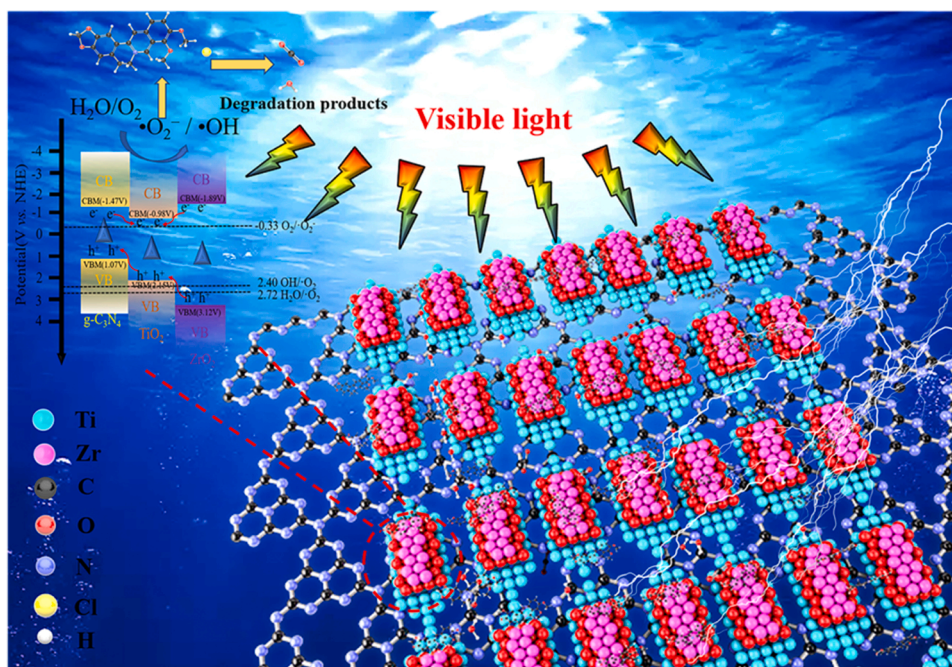


Fig. 9. Schematic of charge transfer in the photocatalytic degradation of BH by the TZCN ternary composites.

Taken together, the results of the simulation experiments and Box-Behnken theoretical predictions suggest that the efficiency of the photocatalytic removal of BH by TZCN was negatively affected by inorganic anions. In actual water environment, such unfavorable effects of coexisting anions can be mitigated by extending the photocatalytic illumination time or/and changing the catalyst dosage [84].

3.3. Mechanism and pathways of photocatalytic degradation of BH

3.3.1. Mechanistic analysis of BH photocatalytic degradation

Quenching studies were then conducted to explore the contributions of free radicals to the photocatalytic degradation of BH. BQ, AO and IPA were added to the reaction solution as specific quenchers of $O_2^{\bullet-}$, h^+ , and $\cdot OH$, respectively. From Fig. 8a and b, one can observe that the addition of AO hardly affects the dynamics of BH degradation, with a removal rate of 84.91% after 60 min's visible light irradiation, in comparison to 86.93% without AO, indicating that h^+ was unlikely to be responsible for BH degradation. By sharp contrast, upon the addition of IPA and BQ, the breakdown of BH was significantly suppressed, with the degradation efficiency markedly reduced to only 51.13% and 18.91%, respectively. This indicates that $O_2^{\bullet-}$ made the major contribution to photocatalytic degradation of BH, with a minor contribution from $\cdot OH$.

These radicals were indeed detected in ESR measurements using 5,5-dimethyl-1-pyrroline-N-oxide (DMPO) as the radical trap. From Fig. 8c and d, one can see that the TCN, TZCN-1 and TZCN-5 samples produced only featureless ESR response in the dark, whereas under Xenon lamp irradiation ($\lambda > 420$ nm), clearly-defined signals can be observed within the range of 3480 to 3540 G, due to the DMPO- $O_2^{\bullet-}$ (Fig. 8e) and DMPO- $\cdot OH$ (Fig. 8f) adducts. Note that as $\cdot OH$ reacts easily with alcohol and becomes inactivated, the $\cdot OH$ radicals were captured by DMPO in water; whereas the DMPO- $O_2^{\bullet-}$ adducts were formed in methanol, because of high reactivity of $O_2^{\bullet-}$ with water but not with alcohol [85,86]. Significantly, the peak-to-peak amplitudes of the $O_2^{\bullet-}$ and $\cdot OH$ radicals were the strongest with the TZCN-1 sample, consistent with the best photocatalytic performance among the series (Fig. 6).

The production of such radical species is most likely facilitated by the formation of heterojunctions within the nanocomposites [87–91], which consisted of type I heterojunctions between TiO_2 and ZrO_2 [24] and type II heterojunctions by TiO_2 and $g-C_3N_4$ (Fig. 9) [31].

Mechanistically, upon visible light irradiation, electrons on the VB of $g-C_3N_4$, TiO_2 and ZrO_2 are excited to their respective CB, thereby generating electron-hole pairs. With the CBM of TiO_2 , ZrO_2 and $g-C_3N_4$ at -0.98, -1.89 and -1.47 V, respectively, the CB electrons of ZrO_2 and $g-C_3N_4$ can be transferred to TiO_2 ; concurrently, with the respective VBM of TiO_2 , ZrO_2 and $g-C_3N_4$ at 2.15, 3.12 and 1.07 V, the transfer of h^+ from TiO_2 and ZrO_2 to $g-C_3N_4$ occurred. Such interfacial charge transfer facilitated the separation of photogenerated electron-hole pairs. From Fig. 9, one can see that the VBM of $g-C_3N_4$ (1.07 V) is less positive than the redox potentials of $H_2O/\cdot OH$ (2.72 V) and $OH/\cdot OH$ (2.40 V) [92, 93], suggesting that the h^+ of $g-C_3N_4$ cannot directly oxidize OH^- or water to $\cdot OH$. However, the CBM of TiO_2 (-0.98 V) is more negative than that of $O_2/O_2^{\bullet-}$ (-0.33 V), suggesting that the photogenerated electrons can readily reduce dissolved oxygen (O_2) in the aqueous solution to produce $O_2^{\bullet-}$ radicals, which are then converted to HO_2^{\bullet} and further to $\cdot OH$ [94,95]. These free radicals are ultimately responsible for the oxidative degradation of BH, as observed experimentally (Fig. 8).

The addition of ZrO_2 may also increase the surface acidity of the nanocomposites in the form of OH groups, thereby facilitate the migration of electrons and holes, and enhance the quantum efficiency [25,96].

3.3.2. Degradation pathways of BH and DFT calculations

To resolve the photocatalytic pathways of BH degradation, the reaction intermediates/products were identified by LC-MS analysis (Fig. 10 and S9). Moreover, the Fukui index (f^0) was computed to identify the vulnerable atomic sites of the BH molecule for radical attack [36,37]. From Fig. 10b and c, the C1 (0.114) and C7 (0.0615) sites can be seen to display a relatively high f^0 value. Based on the Fukui index and in conjunction with the reaction intermediates resolved by LC-MS measurements (Fig. S9), the possible reaction pathways of BH degradation were shown in Fig. 10a. Firstly, BH ($m/z = 336$) produces three isomers ($m/z = 338$) in the photocatalytic reaction, which follow three different degradation pathways. In the first pathway, the $m/z = 338$ isomer is formed by breaking the pyridine ring in the BH molecule. Then, by a second ring-opening reaction at OCH_2O and $O_2^{\bullet-}$ attack of C7, the methyl groups are lost producing an intermediate of $m/z = 200$. Further ring-opening reactions and loss of the methyl groups lead to the generation of intermediates at $m/z = 124$ and 110.

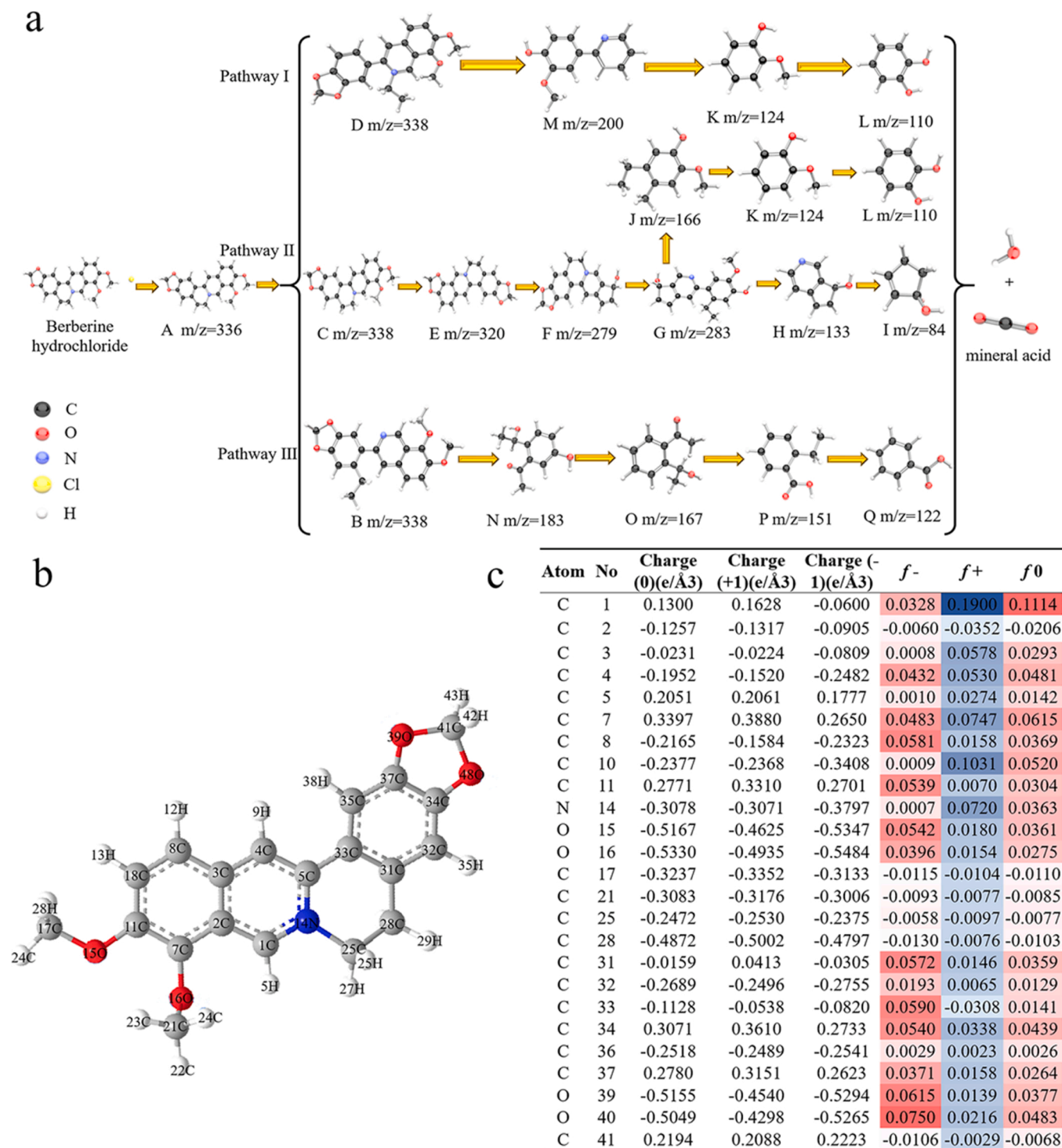


Fig. 10. (a) Photocatalytic degradation pathway of BH by TZCN-1. (b) BH chemical structure. (c) Condensed Fukui index (*f*⁰) of BH.

In the second pathway, the *m/z* = 338 isomer is derived from the hydrogenation reaction of BH (*m/z* = 336). The *m/z* = 320 intermediate is then produced by the loss of a methyl group and post-ring-opening rearrangement reaction. The *m/z* = 279 intermediate is generated from the *m/z* = 320 intermediate through a ring-opening reaction at OCH₂O and elimination of C = O. Subsequently, the C1 site (with the highest Fukui index) is attacked by superoxide radicals, leading to further ring-opening and the formation of an intermediate at *m/z* = 283, which is further cracked to the *m/z* = 166 species. This *m/z* = 166 intermediate then produces *m/z* = 124 and further to *m/z* = 110 after the

loss of the ethyl and methyl groups. Meanwhile, an intermediate of *m/z* = 133 can also be produced from *m/z* = 283 by ring-opening and loss of the methyl and ethyl groups, further decayed to the *m/z* = 84 species.

In the third pathway, the *m/z* = 338 isomer is produced by ring-opening reaction of the NH molecule due to O₂⁻ attack of the C1 site in the BH molecule, and the subsequent pyridine and OCH₂O ring-opening reactions lead to the generation of the *m/z* = 338 intermediate. This intermediate then produces the *m/z* = 167 intermediate after the loss of the hydroxyl group. Further losses of the hydroxyl and methyl groups leads to the formation of the intermediates of *m/z* = 152 and 122

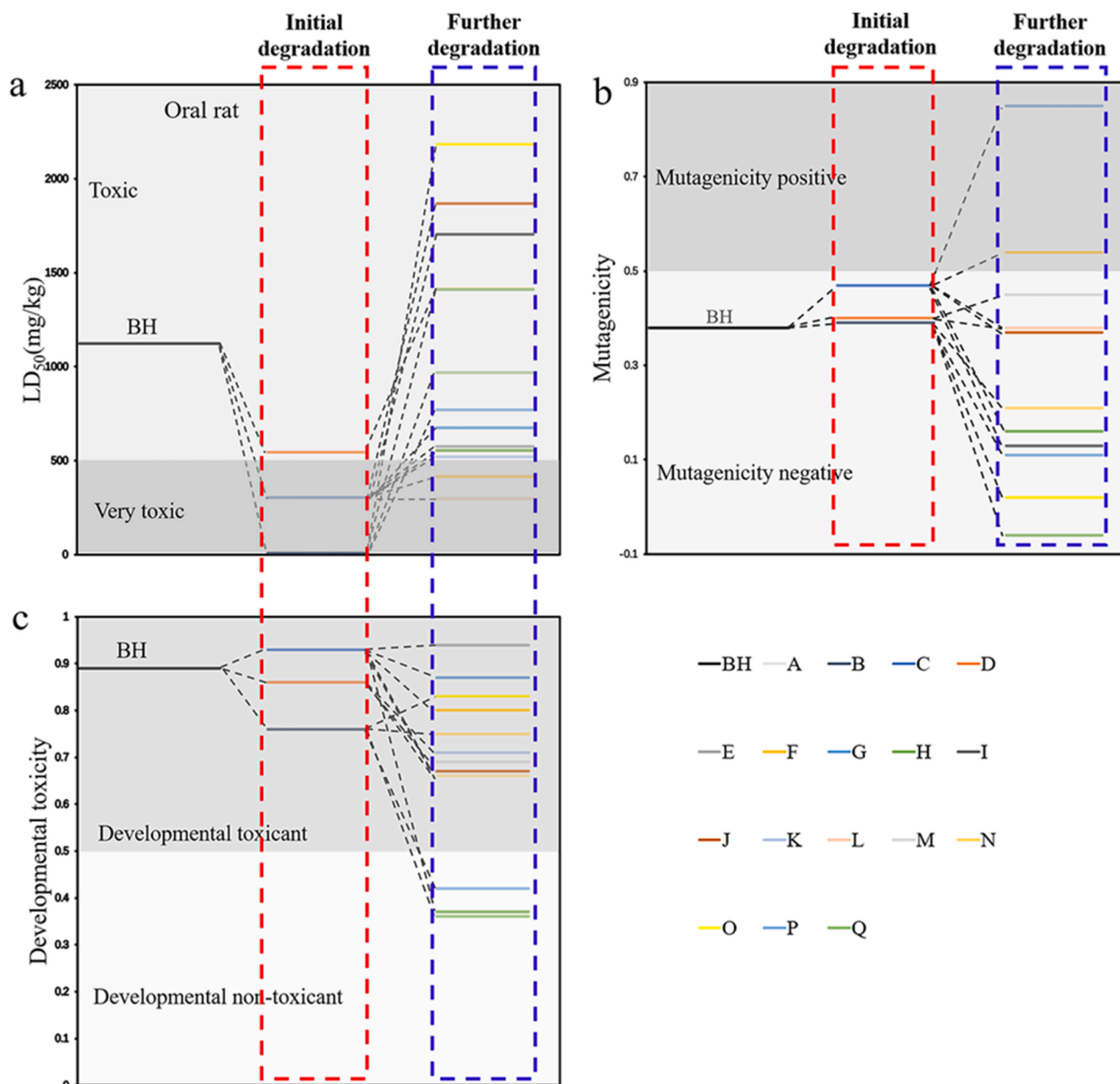


Fig. 11. (a) Oral LD_{50} for rat, (b) mutagenicity and (c) development toxicity of BH and photodegradation intermediates.

[34,97–101].

As the photocatalytic reaction continues, these small intermediates ($m/z = 122, 110$, and 84) will eventually be decomposed into H_2O , CO_2 , and other inorganic substances. The characteristic peak of BH (Fig. S9) gradually decreased, indicating the effective photocatalytic performance of TZCN-1 for BH degradation.

3.3.3. Ecotoxicity analysis of BH intermediates in photodegradation process

TEST and QSAR analyses were then performed to examine the ecotoxicity of the BH degradation intermediates (details in the Supplementary Information), where the lethal dose (LD_{50}), mutagenicity and developmental toxicity of BH and byproducts (A–Q) generated in the photodegradation process were analyzed and compared [102,103]. From Fig. 11a, the oral LD_{50} of BH was found to be at the "toxic" level for rats at ca. $1121.57 \text{ mg kg}^{-1}$. The degradation intermediates produced after the initial attack by free radicals generated three isomers (B, C, and D) that were more toxic than BH, and the oral LD_{50} of A and B can be seen to reach the "very toxic" level. Yet, with the cleavage of the benzene

and pyridine rings, the toxicity was significantly decreased, $2183.61 \text{ mg kg}^{-1}$ for O, $1869.56 \text{ mg kg}^{-1}$ for J, $1703.54 \text{ mg kg}^{-1}$ for I, and $1412.27 \text{ mg kg}^{-1}$ for M, as compared to that of BH. Fig. 11b shows that in the initial stage of TZCN photocatalytic removal of BH, the mutagenicity level of B, C, and D was more positive than that of the BH itself, but as the degradation of BH progressed, the majority of the intermediates appeared at the negative mutagenicity level (< 0.5). Furthermore, except for B and H, most intermediates possessed a lower developmental toxicity than BH, and the intermediates H, Q, and K were even listed as "developmental non-toxicity" (Fig. 11c). That is, although the intermediate toxicity during the initial stage of BH degradation exceeded that of BH, it became markedly reduced in further degradation. These results show that this photocatalytic reaction can not only effectively eliminate BH, but also reduce potential secondary pollution to the water environment that has been known to be caused by the biological toxicity of degradation intermediates.

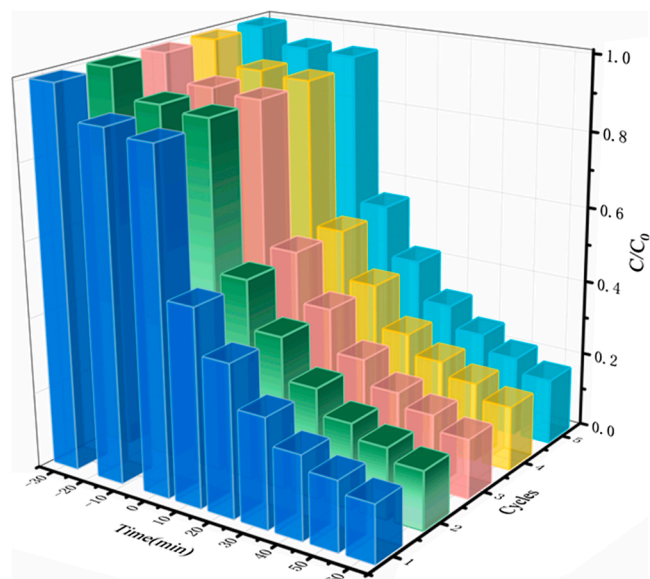


Fig. 12. Photocatalytic degradation removal of BH by TZCN-1 in five consecutive cycles.

3.4. Recycling test

The durability of the photocatalysts is another critical parameter in practical applications. Fig. 12 depicts five consecutive photocatalytic experiments under the same experimental conditions. One can see that TZCN-1 retained the excellent photocatalytic activity, with the degradation efficiency decreased by only 5% in the five consecutive cycles. Notably, there was virtually no change of the XRD patterns (Fig. S10a), XPS profiles (Fig. S10b) and cyclic voltammograms (Fig. S10c) before and after the repeated photodegradation tests. All in all, these test results show that TZCN-1 nanocomposite possessed high stability and reusability.

4. Conclusions

Ternary TZCN nanocomposites were prepared via a facile hydrothermal procedure. In this series, the TZCN-1 sample prepared with a 9:1 Ti:Zr molar feed ratio was found to possess the highest specific surface area ($188.65 \text{ m}^2 \text{ g}^{-1}$), smallest bandgap (2.48 eV), greatest photocurrent, and lowest charge-transfer resistance. This was accounted for by the formation of heterojunctions that promoted the migration, extended the lifetime and enhanced the separation of photoproduced charge carriers. Scavenger quenching experiments and ESR measurements confirmed that the photocatalytic activity was largely ascribed to superoxide radicals, with a minor contribution from hydroxy radicals. On the basis of LC-MS analysis of the degradation intermediates/products and DFT calculations of the Fukui index, the photocatalytic degradation pathways of BH were then proposed, which mainly entailed ring-opening reactions initiated by radical attacks at specific atomic sites within the BH molecules. Furthermore, TZCN could effectively reduce the ecotoxicity of BH in the photocatalytic degradation and avoid secondary pollution of the intermediates to the environment. With the high photocatalytic activity and remarkable durability, the TZCN nanocomposites demonstrate a high potential for practical applications in antibiotic removal from wastewater.

CRediT authorship contribution statement

Peiren Ding and Haodong Ji: execution of research work, data acquisition and analysis, initial drafting of paper. Peishen Li, Yunyun Wu, Ming Guo, Ziang Zhou, Shuai Gao, Wenlu Xu: assistance in data

acquisition, results discussion. Qiming Liu: assistance in data analysis and paper editing. Wen Liu: assistance in data analysis and paper editing. Qiang Wang: conception of research project, paper editing and finalization, research funding. Shaowei Chen: data analysis and organization, paper editing and finalization

Declaration of Competing Interest

The authors declare that they have no known competing financial interests or personal relationships that could have appeared to influence the work reported in this paper.

Acknowledgments

S.W.C. acknowledges partial support of the work by the National Science Foundation (CBET-1848841).

Appendix A. Supplementary data

Supplementary data associated with this article can be found, in the online version, at <https://doi.org/10.1016/j.apcatb.2021.120633>.

References

- [1] J.L. Liu, M.H. Wong, Pharmaceuticals and personal care products (PPCPs): a review on environmental contamination in China, *Environ. Int* 59 (2013) 208–224.
- [2] Q. Zeng, L. Lyu, Y. Gao, S. Chang, C. Hu, A self-sustaining monolithic photoelectrocatalytic/photovoltaic system based on a $\text{WO}_3/\text{BiVO}_4$ photoanode and Si PVC for efficiently producing clean energy from refractory organics degradation, *Appl. Catal. B: Environ.* 238 (2018) 309–317.
- [3] H.B. Quesada, A.T.A. Baptista, L.F. Cusioli, D. Seibert, C. de Oliveira Bezerra, R. Bergamasco, Surface water pollution by pharmaceuticals and an alternative of removal by low-cost adsorbents: A review, *Chemosphere* 222 (2019) 766–780.
- [4] G. Qiu, Y. Song, P. Zeng, L. Duan, S. Xiao, Combination of upflow anaerobic sludge blanket (UASB) and membrane bioreactor (MBR) for berberine reduction from wastewater and the effects of berberine on bacterial community dynamics, *J. Hazard. Mater.* 246–247 (2013) 34–43.
- [5] I.A. Lee, Y.J. Hyun, D.H. Kim, Berberine ameliorates TNBS-induced colitis by inhibiting lipid peroxidation, enterobacterial growth and NF- κ B activation, *Eur. J. Pharmacol.* 648 (2010) 162–170.
- [6] P. Bhutada, Y. Mundhada, K. Bansod, S. Tawari, S. Patil, P. Dixit, S. Umathe, D. Mundhada, Protection of cholinergic and antioxidant system contributes to the effect of berberine ameliorating memory dysfunction in rat model of streptozotocin-induced diabetes, *Behav. Brain. Res.* 220 (2011) 30–41.
- [7] Y. Hu, G.E. Davies, Berberine inhibits adipogenesis in high-fat diet-induced obesity mice, *Fitoterapia* 81 (2010) 358–366.
- [8] V. Homem, L. Santos, Degradation and removal methods of antibiotics from aqueous matrices—a review, *J. Environ. Manage.* 92 (2011) 2304–2347.
- [9] K.J. Choi, S.G. Kim, S.H. Kim, Removal of antibiotics by coagulation and granular activated carbon filtration, *J. Hazard. Mater.* 151 (2008) 38–43.
- [10] S. Agarwal, I. Tyagi, V.K. Gupta, M. Sohrabi, S. Mohammadi, A.N. Golikand, A. Fakhri, Iron doped $\text{SnO}_2/\text{Co}_3\text{O}_4$ nanocomposites synthesized by sol-gel and precipitation method for metronidazole antibiotic degradation, *Mater. Sci. Eng. C Mater. Biol. Appl.* 70 (2017) 178–183.
- [11] J.J. Zheng, S. Kusaka, R. Matsuda, S. Kitagawa, S. Sakaki, Theoretical Insight into Gate-Opening Adsorption Mechanism and Sigmoidal Adsorption Isotherm into Porous Coordination Polymer, *J. Am. Chem. Soc.* 140 (2018) 13958–13969.
- [12] Y.H. Chuang, S. Chen, C.J. Chinn, W.A. Mitch, Comparing the UV/ Monochloramine and UV/Free Chlorine Advanced Oxidation Processes (AOPs) to the UV/Hydrogen Peroxide AOP Under Scenarios Relevant to Potable Reuse, *Environ. Sci. Technol.* 51 (2017) 13859–13868.
- [13] M. Yan, Y. Hua, F. Zhu, W. Gu, J. Jiang, H. Shen, W. Shi, Fabrication of nitrogen doped graphene quantum dots-BiOI/ MnNb_2O_6 p-n junction photocatalysts with enhanced visible light efficiency in photocatalytic degradation of antibiotics, *Appl. Catal. B: Environ.* 202 (2017) 518–527.
- [14] S.S. Chin, T.M. Lim, K. Chiang, A.G. Fane, Factors affecting the performance of a low-pressure submerged membrane photocatalytic reactor, *Chem. Eng. J.* 130 (2007) 53–63.
- [15] M. Mehrjouei, S. Müller, D. Möller, A review on photocatalytic ozonation used for the treatment of water and wastewater, *Chem. Eng. J.* 263 (2015) 209–219.
- [16] M. Pelaez, N.T. Nolan, S.C. Pillai, M.K. Seery, P. Falaras, A.G. Kontos, P.S. M. Dunlop, J.W.J. Hamilton, J.A. Byrne, K. O'Shea, M.H. Entezari, D. Dionysiou, A review on the visible light active titanium dioxide photocatalysts for environmental applications, *Appl. Catal. B: Environ.* 125 (2012) 331–349.
- [17] G. Liu, H.G. Yang, J. Pan, Y.Q. Yang, G.Q. Lu, H.M. Cheng, Titanium dioxide crystals with tailored facets, *Chem. Rev.* 114 (2014) 9559–9612.

- [18] E.M. Samsudin, S.B. Abd Hamid, J.C. Juan, W.J. Basirun, G. Centi, Synergetic effects in novel hydrogenated F-doped TiO₂ photocatalysts, *Appl. Surf. Sci.* 370 (2016) 380–393.
- [19] X. Wu, S. Yin, Q. Dong, T. Sato, Blue/green/red colour emitting up-conversion phosphors coupled C-TiO₂ composites with UV, visible and NIR responsive photocatalytic performance, *Appl. Catal. B: Environ.* 156–157 (2014) 257–264.
- [20] K. Wang, T. Peng, Z. Wang, H. Wang, X. Chen, W. Dai, X. Fu, Correlation between the H₂ response and its oxidation over TiO₂ and N doped TiO₂ under UV irradiation induced by Fermi level, *Appl. Catal. B: Environ.* 250 (2019) 89–98.
- [21] A. Payan, A. Akbar Isari, N. Gholizade, Catalytic decomposition of sulfamethazine antibiotic and pharmaceutical wastewater using Cu-TiO₂@functionalized SWCNT ternary porous nanocomposite: Influential factors, mechanism, and pathway studies, *Chem. Eng. J.* 361 (2019) 1121–1141.
- [22] W. Zhao, L. Feng, R. Yang, J. Zheng, X. Li, Synthesis, characterization, and photocatalytic properties of Ag modified hollow SiO₂/TiO₂ hybrid microspheres, *Appl. Catal. B: Environ.* 103 (2011) 181–189.
- [23] Q. Wang, K. Edalat, Y. Koganemaru, S. Nakamura, M. Watanabe, T. Ishihara, Z. Horita, Photocatalytic hydrogen generation on low-bandgap black zirconia (ZrO₂) produced by high-pressure torsion, *J. Mater. Chem. A* 8 (2020) 3643–3650.
- [24] J. Zhang, L. Li, Z. Xiao, D. Liu, S. Wang, J. Zhang, Y. Hao, W. Zhang, Hollow Sphere TiO₂-ZrO₂ Prepared by Self-Assembly with Polystyrene Colloidal Template for Both Photocatalytic Degradation and H₂ Evolution from Water Splitting, *ACS Appl. Mater. Interfaces* 4 (2016) 2037–2046.
- [25] M. Li, S. Zhang, L. Lv, M. Wang, W. Zhang, B. Pan, A thermally stable mesoporous ZrO₂-CeO₂-TiO₂ visible light photocatalyst, *Chem. Eng. J.* 229 (2013) 118–125.
- [26] Y.Y. Gurkan, E. Kasapbas, Z. Cinar, Enhanced solar photocatalytic activity of TiO₂ by selenium(IV) ion-doping: Characterization and DFT modeling of the surface, *Chem. Eng. J.* 214 (2013) 34–44.
- [27] Q. Xu, C. Jiang, B. Cheng, J. Yu, Enhanced visible-light photocatalytic H₂-generation activity of carbon/g-C₃N₄ nanocomposites prepared by two-step thermal treatment, *Dalton Trans.* 46 (2017) 10611–10619.
- [28] M. Zhang, W. Jiang, D. Liu, J. Wang, Y. Liu, Y. Zhu, Y. Zhu, Photodegradation of phenol via C₃N₄-agar hybrid hydrogel 3D photocatalysts with free separation, *Appl. Catal. B: Environ.* 183 (2016) 263–268.
- [29] H. Zhang, L. Zhao, F. Geng, L.-H. Guo, B. Wan, Y. Yang, Carbon dots decorated graphitic carbon nitride as an efficient metal-free photocatalyst for phenol degradation, *Appl. Catal. B: Environ.* 180 (2016) 656–662.
- [30] W. Wang, J.C. Yu, D. Xia, P.K. Wong, Y. Li, Graphene and g-C₃N₄ nanosheets copropagated elemental alpha-sulfur as a novel metal-free heterojunction photocatalyst for bacterial inactivation under visible-light, *Environ. Sci. Technol.* 47 (2013) 8724–8732.
- [31] W. Wang, J. Fang, S. Shao, M. Lai, C. Lu, Compact and uniform TiO₂@g-C₃N₄ core-shell quantum heterojunction for photocatalytic degradation of tetracycline antibiotics, *Appl. Catal. B: Environ.* 217 (2017) 57–64.
- [32] Z. Lu, L. Zeng, W. Song, Z. Qin, D. Zeng, C. Xie, In situ synthesis of C-TiO₂/g-C₃N₄ heterojunction nanocomposite as highly visible light active photocatalyst originated from effective interfacial charge transfer, *Appl. Catal. B: Environ.* 202 (2017) 489–499.
- [33] Z. Tong, D. Yang, T. Xiao, Y. Tian, Z. Jiang, Biomimetic fabrication of g-C₃N₄/TiO₂ nanosheets with enhanced photocatalytic activity toward organic pollutant degradation, *Chem. Eng. J.* 260 (2015) 117–125.
- [34] Y. Yu, W. Xu, J. Fang, D. Chen, T. Pan, W. Feng, Y. Liang, Z. Fang, Soft-template assisted construction of superstructure TiO₂/SiO₂/g-C₃N₄ hybrid as efficient visible-light photocatalysts to degrade berberine in seawater via an adsorption-photocatalysis synergy and mechanism insight, *Appl. Catal. B: Environ.* 268 (2020), 118751.
- [35] K. Rabé, L. Liu, N.A. Nahyoon, Y. Zhang, A.M. Idris, Visible-light photocatalytic fuel cell with Z-scheme g-C₃N₄/Fe³⁺/TiO₂ anode and WO₃ cathode efficiently degrades berberine chloride and stably generates electricity, *Sep. Purif. Technol.* 212 (2019) 774–782.
- [36] W. Liu, Y. Li, F. Liu, W. Jiang, D. Zhang, J. Liang, Visible-light-driven photocatalytic degradation of diclofenac by carbon quantum dots modified porous g-C₃N₄: Mechanisms, degradation pathway and DFT calculation, *Water Res.* 150 (2019) 431–441.
- [37] C. Zhao, Z. Liao, W. Liu, F. Liu, J. Ye, J. Liang, Y. Li, Carbon quantum dots modified tubular g-C₃N₄ with enhanced photocatalytic activity for carbamazepine elimination: Mechanisms, degradation pathway and DFT calculation, *J. Hazard. Mater.* 381 (2020), 120957.
- [38] T. Lu, F. Chen, Multiwfn: a multifunctional wavefunction analyzer, *J. Comput. Chem.* 33 (2012) 580–592.
- [39] Y. Deng, L. Tang, C. Peng, G. Zeng, Z. Chen, J. Wang, H. Feng, B. Peng, Y. Liu, Y. Zhou, Insight into the dual-channel charge-carrier transfer path for nonmetal plasmonic tungsten oxide based composites with boosted photocatalytic activity under full-spectrum light, *Appl. Catal. B: Environ.* 235 (2018) 225–237.
- [40] J. Qin, H. Zeng, Photocatalysts fabricated by depositing plasmonic Ag nanoparticles on carbon quantum dots/graphitic carbon nitride for broad spectrum photocatalytic hydrogen generation, *Appl. Catal. B: Environ.* 209 (2017) 161–173.
- [41] J. Ma, C. Wang, H. He, Enhanced photocatalytic oxidation of NO over g-C₃N₄-TiO₂ under UV and visible light, *Appl. Catal. B: Environ.* 184 (2016) 28–34.
- [42] C.V. Reddy, B. Babu, I.N. Reddy, J. Shim, Synthesis and characterization of pure tetragonal ZrO₂ nanoparticles with enhanced photocatalytic activity, *Ceram. Int.* 44 (2018) 6940–6948.
- [43] Y. Zhang, Y. Zhao, T. Otroshchenko, S. Han, H. Lund, U. Rodemerck, D. Linke, H. Jiao, G. Jiang, E.V. Kondratenko, The effect of phase composition and crystallite size on activity and selectivity of ZrO₂ in non-oxidative propane dehydrogenation, *J. Catal.* 371 (2019) 313–324.
- [44] S. Shao, A.-W. Shi, C.-L. Liu, R.-Z. Yang, W.-S. Dong, Hydrogen production from steam reforming of glycerol over Ni/CeZrO catalysts, *Fuel Process Technol.* 125 (2014) 1–7.
- [45] Z. Li, R. Wnetrzak, W. Kwapiński, J.J. Leahy, Synthesis and characterization of sulfated TiO₂ nanorods and ZrO₂/TiO₂ nanocomposites for the esterification of biobased organic acid, *ACS Appl. Mater. Interfaces* 4 (2012) 4499–4505.
- [46] L. Ma, G. Wang, C. Jiang, H. Bao, Q. Xu, Synthesis of core-shell TiO₂@g-C₃N₄ hollow microspheres for efficient photocatalytic degradation of rhodamine B under visible light, *Appl. Surf. Sci.* 430 (2018) 263–272.
- [47] J. Ma, X. Tan, T. Yu, X. Li, Fabrication of g-C₃N₄/TiO₂ hierarchical spheres with reactive {001} TiO₂ crystal facets and its visible-light photocatalytic activity, *Int. J. Hydrogen Energy* 41 (2016) 3877–3887.
- [48] M. Xu, L. Han, S. Dong, Facile fabrication of highly efficient g-C₃N₄/Ag₂O heterostructured photocatalysts with enhanced visible-light photocatalytic activity, *ACS Appl. Mater. Interfaces* 5 (2013) 12533–12540.
- [49] W. Yu, D. Xu, T. Peng, Enhanced photocatalytic activity of g-C₃N₄ for selective CO₂ reduction to CH₃OH via facile coupling of ZnO: a direct Z-scheme mechanism, *J. Mater. Chem. A* 3 (2015) 19936–19947.
- [50] Y. Li, H. Zhang, P. Liu, D. Wang, Y. Li, H. Zhao, Cross-linked g-C₃N₄/rGO nanocomposites with tunable band structure and enhanced visible light photocatalytic activity, *Small* 9 (2013) 3336–3344.
- [51] J. Tian, Q. Shao, J. Zhao, D. Pan, M. Dong, C. Jia, T. Ding, T. Wu, Z. Guo, Microwave solvothermal carboxymethyl chitosan templated synthesis of TiO₂/ZrO₂ composites toward enhanced photocatalytic degradation of Rhodamine B, *J. Colloid Interface Sci.* 541 (2019) 18–29.
- [52] Z.-a. Huang, Q. Sun, K. Lv, Z. Zhang, M. Li, B. Li, Effect of contact interface between TiO₂ and g-C₃N₄ on the photoreactivity of g-C₃N₄/TiO₂ photocatalyst: (0 0 1) vs (1 0 1) facets of TiO₂, *Appl. Catal. B: Environ.* 164 (2015) 420–427.
- [53] R. Hao, G. Wang, H. Tang, L. Sun, C. Xu, D. Han, Template-free preparation of macro/mesoporous g-C₃N₄/TiO₂ heterojunction photocatalysts with enhanced visible light photocatalytic activity, *Appl. Catal. B: Environ.* 187 (2016) 47–58.
- [54] W. Zhang, X. Xiao, Y. Li, X. Zeng, L. Zheng, C. Wan, Liquid-exfoliation of layered MoS₂ for enhancing photocatalytic activity of TiO₂/g-C₃N₄ photocatalyst and DFT study, *Appl. Surf. Sci.* 389 (2016) 496–506.
- [55] Y. Wang, L. Rao, P. Wang, Z. Shi, L. Zhang, Photocatalytic activity of N-TiO₂/O-doped N vacancy g-C₃N₄ and the intermediates toxicity evaluation under tetracycline hydrochloride and Cr(VI) coexistence environment, *Appl. Catal. B: Environ.* 262 (2020), 118308.
- [56] S.H. Liu, W.X. Lin, A simple method to prepare g-C₃N₄-TiO₂/waste zeolites as visible-light-responsive photocatalytic coatings for degradation of indoor formaldehyde, *J. Hazard. Mater.* 368 (2019) 468–476.
- [57] J. Zhao, S. Ge, D. Pan, Q. Shao, J. Lin, Z. Wang, Z. Hu, T. Wu, Z. Guo, Solvothermal synthesis, characterization and photocatalytic property of zirconium dioxide doped titanium dioxide spinous hollow microspheres with sunflower pollen as bio-templates, *J. Colloid Interface Sci.* 529 (2018) 111–121.
- [58] M. Huang, Y. Zhang, Y. Zhou, C. Zhang, S. Zhao, J. Fang, Y. Gao, S. Sheng, Preparation of TiO₂-ZrO₂/Au/CeO₂ hollow sandwich-like nanostructures for excellent catalytic activity and thermal stability, *New. J. Chem.* 41 (2017) 13472–13482.
- [59] M. Li, X. Li, G. Jiang, G. He, Hierarchically macro-mesoporous ZrO₂-TiO₂ composites with enhanced photocatalytic activity, *Ceram. Int.* 41 (2015) 5749–5757.
- [60] M. Hu, Z. Xing, Y. Cao, Z. Li, X. Yan, Z. Xiu, T. Zhao, S. Yang, W. Zhou, Ti³⁺ self-doped mesoporous black TiO₂/SiO₂/g-C₃N₄ sheets heterojunctions as remarkable visible-light-driven photocatalysts, *Appl. Catal. B: Environ.* 226 (2018) 499–508.
- [61] K. Li, Z. Huang, X. Zeng, B. Huang, S. Gao, J. Lu, Synergetic Effect of Ti(3+) and Oxygen Doping on Enhancing Photoelectrochemical and Photocatalytic Properties of TiO₂/g-C₃N₄ Heterojunctions, *ACS Appl. Mater. Interfaces* 9 (2017) 11577–11586.
- [62] W. Zheng, Z. Yan, Y. Dai, N. Du, X. Jiang, H. Dai, X. Li, G. He, Interpenetrated Networks between Graphitic Carbon Infilling and Ultrafine TiO₂ Nanocrystals with Patterned Macroporous Structure for High-Performance Lithium Ion Batteries, *ACS Appl. Mater. Interfaces* 9 (2017) 20491–20500.
- [63] G. Zhang, G. Li, Z.A. Lan, L. Lin, A. Savateev, T. Heil, S. Zafeirotas, X. Wang, M. Antonietti, Optimizing Optical Absorption, Exciton Dissociation, and Charge Transfer of a Polymeric Carbon Nitride with Ultrahigh Solar Hydrogen Production Activity, *Angew. Chem. Int. Ed.* 56 (2017) 13445–13449.
- [64] Y. Tan, Z. Shu, J. Zhou, T. Li, W. Wang, Z. Zhao, One-step synthesis of nanostructured g-C₃N₄/TiO₂ composite for highly enhanced visible-light photocatalytic H₂ evolution, *Appl. Catal. B: Environ.* 230 (2018) 260–268.
- [65] Y.C. Zhang, M. Yang, G. Zhang, D.D. Dionysiou, HNO₃-involved one-step low temperature solvothermal synthesis of N-doped TiO₂ nanocrystals for efficient photocatalytic reduction of Cr(VI) in water, *Appl. Catal. B: Environ.* 142–143 (2013) 249–258.
- [66] Y. Zhang, L. Wu, X. Zhao, Y. Zhao, H. Tan, X. Zhao, Y. Ma, Z. Zhao, S. Song, Y. Wang, Y. Li, Leaf-Mosaic-Inspired Vine-Like Graphitic Carbon Nitride Showing High Light Absorption and Efficient Photocatalytic Hydrogen Evolution, *Adv. Energy Mater.* 8 (2018), 1801139.
- [67] K. Chang, X. Hai, H. Pang, H. Zhang, L. Shi, G. Liu, H. Liu, G. Zhao, M. Li, J. Ye, Targeted Synthesis of 2H- and 1T-Phase MoS₂ Monolayers for Catalytic Hydrogen Evolution, *Adv. Mater.* 28 (2016) 10033–10041.
- [68] H. Yu, R. Shi, Y. Zhao, T. Bian, Y. Zhao, C. Zhou, G.I.N. Waterhouse, L.Z. Wu, C. H. Tung, T. Zhang, Alkali-Assisted Synthesis of Nitrogen Deficient Graphitic

- Carbon Nitride with Tunable Band Structures for Efficient Visible-Light-Driven Hydrogen Evolution, *Adv. Mater.* 29 (2017).
- [69] Y. Li, W. Cui, L. Liu, R. Zong, W. Yao, Y. Liang, Y. Zhu, Removal of Cr(VI) by 3D TiO₂-graphene hydrogel via adsorption enriched with photocatalytic reduction, *Appl. Catal. B: Environ.* 199 (2016) 412–423.
- [70] D. Chen, J. Liu, Z. Jia, J. Fang, F. Yang, Y. Tang, K. Wu, Z. Liu, Z. Fang, Efficient visible-light-driven hydrogen evolution and Cr(VI) reduction over porous P and Mo co-doped g-C₃N₄ with feeble N vacancies photocatalyst, *J. Hazard. Mater.* 361 (2019) 294–304.
- [71] T. Giannakopoulou, I. Papailias, N. Todorova, N. Boukos, Y. Liu, J. Yu, C. Trapalis, Tailoring the energy band gap and edges' potentials of g-C₃N₄/TiO₂ composite photocatalysts for NO_x removal, *Chem. Eng. J.* 310 (2017) 571–580.
- [72] X.H. Yi, S.Q. Ma, X.D. Du, C. Zhao, H. Fu, P. Wang, C.C. Wang, The facile fabrication of 2D/3D Z-scheme g-C₃N₄/UiO-66 heterojunction with enhanced photocatalytic Cr(VI) reduction performance under white light, *Chem. Eng. J.* 375 (2019), 121944.
- [73] A. Naldoni, M. Altomare, G. Zoppellaro, N. Liu, S. Kment, R. Zboril, P. Schmuki, Photocatalysis with Reduced TiO₂: From Black TiO₂ to Cocatalyst-Free Hydrogen Production, *ACS Catal.* 9 (2019) 345–364.
- [74] Q. Han, B. Wang, J. Gao, Z. Cheng, Y. Zhao, Z. Zhang, L. Qu, Atomically Thin Mesoporous Nanomesh of Graphitic C₃N₄ for High-Efficiency Photocatalytic Hydrogen Evolution, *ACS Nano* 10 (2016) 2745–2751.
- [75] E. Bailón-García, A. Elmouwahidi, F. Carrasco-Marín, A.F. Pérez-Cadenas, F. J. Maldonado-Hódar, Development of Carbon-ZrO₂ composites with high performance as visible-light photocatalysts, *Appl. Catal. B: Environ.* 217 (2017) 540–550.
- [76] X. Bu, Y. Gao, S. Zhang, Y. Tian, Amorphous cerium phosphate on P-doped Fe₂O₃ nanosheets for efficient photoelectrochemical water oxidation, *Chem. Eng. J.* 355 (2019) 910–919.
- [77] G. Di, Z. Zhu, H. Zhang, J. Zhu, Y. Qiu, D. Yin, S. Kuipers, Visible-light degradation of sulfonamides by Z-scheme ZnO/g-C₃N₄ heterojunctions with amorphous Fe₂O₃ as electron mediator, *J. Colloid Interface Sci.* 538 (2019) 256–266.
- [78] C. Ye, J.-X. Li, Z.-J. Li, X.-B. Li, X.-B. Fan, L.-P. Zhang, B. Chen, C.-H. Tung, L.-Z. Wu, Enhanced Driving Force and Charge Separation Efficiency of Protonated g-C₃N₄ for Photocatalytic O₂ Evolution, *ACS Catal.* 5 (2015) 6973–6979.
- [79] H. Shi, G. Chen, C. Zhang, Z. Zou, Polymeric g-C₃N₄ Coupled with NaNbO₃ Nanowires toward Enhanced Photocatalytic Reduction of CO₂ into Renewable Fuel, *ACS Catal.* 4 (2014) 3637–3643.
- [80] G. Zhang, T. Zhang, B. Li, S. Jiang, X. Zhang, L. Hai, X. Chen, W. Wu, An ingenious strategy of preparing TiO₂/g-C₃N₄ heterojunction photocatalyst: In situ growth of TiO₂ nanocrystals on -C₃N₄ nanosheets via impregnation-calcination method, *Appl. Surf. Sci.* 433 (2018) 963–974.
- [81] X. She, L. Liu, H. Ji, Z. Mo, Y. Li, L. Huang, D. Du, H. Xu, H. Li, Template-free synthesis of 2D porous ultrathin nonmetal-doped g-C₃N₄ nanosheets with highly efficient photocatalytic H₂ evolution from water under visible light, *Appl. Catal. B: Environ.* 187 (2016) 144–153.
- [82] J. Di, J. Xia, M. Ji, S. Yin, H. Li, H. Xu, Q. Zhang, H. Li, Controllable synthesis of Bi₄O₅Br₂ ultrathin nanosheets for photocatalytic removal of ciprofloxacin and mechanism insight, *J. Mater. Chem. A* 3 (2015) 15108–15118.
- [83] C. Wang, L. Zhu, M. Wei, P. Chen, G. Shan, Photolytic reaction mechanism and impacts of coexisting substances on photodegradation of bisphenol A by Bi₂WO₆ in water, *Water. Res.* 46 (2012) 845–853.
- [84] X.H. Yi, H. Ji, C.C. Wang, Y. Li, Y.H. Li, C. Zhao, A. Wang, H. Fu, P. Wang, X. Zhao, W. Liu, Photocatalysis-activated SR-AOP over PDINH/MIL-88A(Fe) composites for boosted chloroquine phosphate degradation: Performance, mechanism, pathway and DFT calculations, *Appl. Catal. B: Environ.* 293 (2021), 120229.
- [85] P. Li, M. Guo, Q. Wang, Z. Li, C. Wang, N. Chen, C. Wang, C. Wan, S. Chen, Controllable synthesis of cerium zirconium oxide nanocomposites and their application for photocatalytic degradation of sulfonamides, *Appl. Catal. B: Environ.* 259 (2019), 118107.
- [86] L. Wang, X. Lan, W. Peng, Z. Wang, Uncertainty and misinterpretation over identification, quantification and transformation of reactive species generated in catalytic oxidation processes: A review, *J. Hazard. Mater.* 408 (2021), 124436.
- [87] L. Wang, X. Guo, Y. Chen, S. Ai, H. Ding, Cobalt-doped g-C₃N₄ as a heterogeneous catalyst for photo-assisted activation of peroxymonosulfate for the degradation of organic contaminants, *Appl. Surf. Sci.* 467–468 (2019) 954–962.
- [88] Z. Mu, S. Chen, Y. Wang, Z. Zhang, Z. Li, B. Xin, L. Jing, Controlled Construction of Copper Phthalocyanine/ α -Fe₂O₃ Ultrathin S-Scheme Heterojunctions for Efficient Photocatalytic CO₂ Reduction under Wide Visible-Light Irradiation, *Small Science* (2021), 2100050.
- [89] F.R. Pomilla, E.I. García-López, G. Marci, L. Palmisano, F. Parrino, Heterogeneous photocatalytic materials for sustainable formation of high-value chemicals in green solvents, *Mater. Today Sustain* 13 (2021), 100071.
- [90] C.-M. Fung, J.-Y. Tang, L.-L. Tan, A.R. Mohamed, S.-P. Chai, Recent progress in two-dimensional nanomaterials for photocatalytic carbon dioxide transformation into solar fuels, *Mater. Today Sustain* 9 (2020), 100037.
- [91] D. Ayodhya, G. Veerabhadram, Stable and efficient graphitic carbon nitride nanosheet-supported ZnS composite catalysts toward competent catalytic performance for the reduction of 4-nitrophenol using NaBH₄, *Mater. Today Sustain* 5 (2019), 100015.
- [92] T. Lv, D. Li, Y. Hong, B. Luo, D. Xu, M. Chen, W. Shi, Facile synthesis of CdS/Bi₄V₂O₁₁ photocatalysts with enhanced visible-light photocatalytic activity for degradation of organic pollutants in water, *Dalton Trans* 46 (2017) 12675–12682.
- [93] H. Ji, P. Du, D. Zhao, S. Li, F. Sun, E.C. Duin, W. Liu, 2D/1D graphitic carbon nitride/titanate nanotubes heterostructure for efficient photocatalysis of sulfamethazine under solar light: Catalytic “hot spots” at the rutile–anatase–titanate interfaces, *Appl. Catal. B: Environ.* 263 (2020).
- [94] W.K. Jo, N. Clament Sagaya Selvam, Enhanced visible light-driven photocatalytic performance of ZnO-g-C₃N₄ coupled with graphene oxide as a novel ternary nanocomposite, *J. Hazard. Mater.* 299 (2015) 462–470.
- [95] W.Y. Teoh, J.A. Scott, R. Amal, Progress in Heterogeneous Photocatalysis: From Classical Radical Chemistry to Engineering Nanomaterials and Solar Reactors, *J. Phys. Chem. Lett.* 3 (2012) 629–639.
- [96] Q. Chen, W. Yang, J. Zhu, L. Fu, D. Li, L. Zhou, Enhanced visible light photocatalytic activity of g-C₃N₄ decorated ZnO nanotubes heterostructure for degradation of tetracycline hydrochloride, *J. Hazard. Mater.* 384 (2020), 121275.
- [97] Y. Zhang, L. Liu, B. Van der Bruggen, M.K.H. Leung, F. Yang, A free-standing 3D nano-composite photo-electrode—Ag/ZnO nanorods arrays on Ni foam effectively degrade berberine, *Chem. Eng. J.* 373 (2019) 179–191.
- [98] J. Radjenovic, M. Petrovic, F. Ventura, D. Barcelo, Rejection of pharmaceuticals in nanofiltration and reverse osmosis membrane drinking water treatment, *Water Res.* 42 (2008) 3601–3610.
- [99] R. Feng, Z.X. Zhao, S.R. Ma, F. Guo, Y. Wang, J.D. Jiang, Gut Microbiota-Regulated Pharmacokinetics of Berberine and Active Metabolites in Beagle Dogs After Oral Administration, *Front. Pharmacol.* 9 (2018) 214.
- [100] M. Abd El-Salam, H. Mekky, E.M.B. El-Naggar, D. Ghareeb, M. El-Demellawy, F. El-Fiky, Hepatoprotective properties and biotransformation of berberine and berberrubine by cell suspension cultures of *Dodonaea viscosa* and *Ocimum basilicum*, *S. Afr. J. Bot.* 97 (2015) 191–195.
- [101] D. Wang, Z. Liu, M. Guo, S. Liu, Structural elucidation and identification of alkaloids in *Rhizoma Coptidis* by electrospray ionization tandem mass spectrometry, *J. Mass Spectrom.* 39 (2004) 1356–1365.
- [102] L. Chen, H. Ji, J. Qi, T. Huang, C. Wang, W. Liu, Degradation of acetaminophen by activated peroxymonosulfate using Co(OH)₂ hollow microsphere supported titanate nanotubes: Insights into sulfate radical production pathway through CoOH⁺ activation, *Chem. Eng. J.* 406 (2021), 126877.
- [103] H. Ji, W. Liu, F. Sun, T. Huang, L. Chen, Y. Liu, J. Qi, C. Xie, D. Zhao, Experimental evidences and theoretical calculations on phenanthrene degradation in a solar-light-driven photocatalysis system using silica aerogel supported TiO₂ nanoparticles: Insights into reactive sites and energy evolution, *Chem. Eng. J.* 419 (2021), 129605.